

TESTING THE GRAVITATIONAL FIELD IN ELLIPTICAL GALAXIES: NGC 5077¹

FRANCESCO BERTOLA

Department of Astronomy, University of Padova, 35122 Padova, Italy

DANIELA BETTONI

Padova Astronomical Observatory, 35100 Padova, Italy

JOHN DANZIGER

European Southern Observatory, D-8046 Garching bei München, Germany

ELAINE SADLER²

Anglo-Australian Observatory, P.O. Box 296, Epping, NSW 2121, Australia

LINDA SPARKE³

Kapteyn Laboratorium

AND

TIM DE ZEEUW⁴

Institute for Advanced Study, and California Institute of Technology

Received 1990 January 2; accepted 1990 November 20

ABSTRACT

NGC 5077 is an elliptical galaxy with a disk of ionized gas along its minor axis. Observations of the structure and kinematics of this gas disk allow us to investigate both the intrinsic shape and the mass distribution of the underlying galaxy.

The rotation axis of the gas disk is displaced by $23^\circ \pm 5^\circ$ from the apparent major axis of the galaxy, so the gas cannot lie in the equatorial plane of an axisymmetric potential. If the galaxy is triaxial and the gas disk has settled into a principal plane then there are two possible configurations, both with the gas on elliptical orbits. One is an oblate triaxial system with the gas in a plane perpendicular to the longest axis, the other is a prolate triaxial galaxy with the gas in the plane perpendicular to the shortest axis. Alternatively, the gas may lie in the warped and precessing polar ring around an oblate galaxy—in this case the gas must have been acquired recently, probably less than 10^9 yr ago.

The observed rotation curve of the gas rises slowly, reaching a peak at $\sim 10''$ from the nucleus. For circular orbits in a spherical potential, this would imply a decrease of M/L toward the center, since the core radius of the light is $1''$ or less. For gas on elliptic orbits, however, the precise shape of the observed rotation curve will depend on the viewing angle. If the gas lies in a warped polar ring, material further out may be seen in projection close to the center so that the observed rotation velocity is much less than the true circular speed.

For NGC 5077, we construct various triaxial and oblate mass models which have constant M/L and are consistent both with the observed velocity fields of gas and stars and with the central mass-to-light ratio implied by the observed stellar velocity dispersion. Thus the slowly rising rotation curve of the gas in NGC 5077 does not require the presence of dark matter in the inner regions.

Subject headings: galaxies: individual (NGC 5077) — galaxies: internal motions — galaxies: structure

1. INTRODUCTION

Photometric and kinematic data are now available for a dozen or more elliptical galaxies with a gas disk or dust lane (for a review, see Bertola 1987). Gas disks are valuable tracers of the gravitational potential in elliptical galaxies, and may give constraints on the intrinsic shape of the underlying galaxy (Merritt & de Zeeuw 1983; Gerhard & Vietri 1986, 1987; de Zeeuw & Franx 1989, hereafter dZF).

However, attempts to use gas disks to measure the mass-to-light ratio M/L of early-type galaxies have produced some puzzling results. Caldwell (1984) drew attention to the slowly rising emission-line rotation curves in two dust-lane elliptical galaxies, NGC 3108 and NGC 5266, and pointed out that central values of M/L derived from the gas rotation velocity were much lower than those implied by typical stellar velocity dispersions. In a study of the elliptical galaxy NGC 7097, Caldwell, Kirshner, & Richstone (1986, hereafter CKR) derived a radial mass distribution $M(r)$ by assuming the gas was on circular orbits in a spherical potential. Comparing this with the luminosity profile, they found an apparent decrease of M/L in the central regions of the galaxy. Fillmore, Boroson, & Dressler (1986) and Kent (1988) have reported a similar effect in several spiral bulges, which suggests it may be a common feature of early-type galaxies.

¹ Based on observations collected at the European Southern Observatory at La Silla (Chile).

² Visiting astronomer at the Cerro Tololo Inter-American Observatory of the NOAO, operated by AURA, Inc., under contract to the National Science Foundation.

³ Present address: Washburn Observatory, University of Wisconsin, Madison, WI 53706.

⁴ Present address: Sterrewacht Leiden, P.O. Box 9513, 2300RA Leiden, The Netherlands.

There are two possible reasons for the slowly rising gas velocities. Either M/L really does decrease in the inner regions of many early-type galaxies (both elliptical and spiral), or gas near the center is not on circular orbits. Fillmore, Boroson & Dressler (1986) showed that changes in M/L were *not* responsible for the slowly rising rotation curves in the spiral bulges they observed, since the observed gas velocities were less than those calculated from the observed stellar velocities at each radius. Kent (1988) suggested that gas in the central regions of some Sa galaxies may have been disturbed, perhaps by supernova heating, while Kormendy & Westpfahl (1989) suggest that the central gas in NGC 4594 may have cooled from an X-ray halo or been shed by slowly rotating bulge stars.

An alternative, and more general, explanation is that elliptical galaxies and spiral bulges are triaxial. If so, gas orbits near the center will generally be elliptical rather than circular, and the observed form of the rotation curve will depend on the direction from which the galaxy is viewed. Recent high-quality spectroscopic observations of the gas in the spiral galaxy NGC 4845 show that this galaxy has a triaxial bulge whose shape can be accurately determined (Bertola, Rubin, & Zeilinger 1989; Gerhard, Vietri, & Kent 1989).

Our aim here is to construct realistic triaxial mass models for early-type galaxies. If we can find models of this kind which are consistent with the observed velocity field of both gas and stars, then it should be possible to determine M/L with some confidence.

To construct a realistic mass model, we must first determine the intrinsic shape of the galaxy to be studied. This cannot be found from a simple deprojection of surface photometry or from the morphology or orientation of a gas disk or dust lane, and measurement of a full two-dimensional velocity field for both gas and stars is generally necessary (dZF).

Here we present a study of the southern elliptical galaxy NGC 5077. This galaxy is the brightest member of a small group at a distance of ~ 56 Mpc ($H_0 = 50 \text{ km s}^{-1} \text{ Mpc}^{-1}$), and is classified E3+ by de Vaucouleurs, de Vaucouleurs, & Corwin (1976) and E3 by Sandage & Tammann (1981). It has a compact central radio source (Heeschen 1970; Ekers & Ekers 1973; Disney & Cromwell 1970; Hummel, Kotanyi, & Ekers 1983; Wrobel & Heeschen 1984) and has long been known to show emission lines (Humason, Mayall, & Sandage 1956). The observed emission line ratios are characteristic of LINERs (e.g., Heckman 1980), suggesting that the gas in NGC 5077 is ionized by nonthermal means rather than in H II regions. The ionized gas has been studied in some detail by Demoulin-Ulrich, Butcher, & Boksenberg (1984, hereafter DBB), who measured the gas rotation velocities at three different position angles and noted that the H α outer isophotes were slightly elongated along the minor axis.

We have extended the coverage of the gas velocity field for NGC 5077 and measured stellar rotation and velocity dispersion profiles as well. We have also used a CCD camera and H α /[N II] filter to map the ionized gas distribution in more detail. We extend the approach taken by CKR, using the gas disk in NGC 5077 as a probe of the gravitational field of the underlying galaxy, but relaxing the assumption that the potential is spherical. If the gas is in equilibrium and lies in a principal plane of the stellar figure, we can set strong constraints on the shape and orientation of the galaxy and we can derive M/L as a function of radius. The same method can be applied to other galaxies, and we briefly discuss some examples from the literature.

In § 2 we discuss our observations, and in § 3 we consider spherical and axisymmetric mass models with the gas on circular orbits in the equatorial plane. In § 4 we discuss triaxial models with the gas in a principal plane, but on elliptic orbits. Models with a gas disk which warps out of a principal plane are constructed in § 5. We briefly discuss some other ellipticals with gas disks in § 6 and summarize our findings in § 7.

We have used $H_0 = 50 \text{ km s}^{-1} \text{ Mpc}^{-1}$ throughout this paper.

2. OBSERVATIONS

2.1. Spectroscopic Observations at ESO

Three spectra of NGC 5077 were taken in 1983 May with the Boller and Chivens spectrograph and image tube at the Cassegrain focus of the ESO 3.6 m telescope. The spectrograph slit was aligned along the major (P.A. 7°), minor (P.A. 97°) and intermediate (P.A. 127°) axes, with exposure times of 90 minutes for the major and minor axis spectra and 40 minutes for the intermediate axis. The spectral dispersion was 39 \AA mm^{-1} , and the plate scale perpendicular to the dispersion $38''.5 \text{ mm}^{-1}$.

On each night, at least two template spectra of slowly rotating giant stars of spectral type from late G to early K were also taken. All the plates were digitized with the ESO PDS microdensitometer and further reduced using the IHAP software package. The resulting images were analyzed at Padova Observatory. The Fourier Quotient technique was first applied to a region around the G band (4000–4500 \AA), then a second reduction was performed with the wavelength interval extended to include the Ca II H and K lines (3900–4500 \AA). This second reduction gives more accurate velocities, but at the same time reduces the accuracy of the dispersion measurements because the intrinsically broad calcium lines are less sensitive than the G band to velocity broadening (Kormendy & Illingworth 1982). In Table 1 and Figure 1, the stellar velocities at P.A. 7° , 97° , and 127° are measured with the H and K lines included, while the stellar velocity dispersion is measured from the 4000–4500 \AA region only.

In addition, the [O II] $\lambda\lambda 3727, 3729 \text{ \AA}$ doublet was measured with the ESO Grant machine to derive the emission-line rotation curve. The resulting velocities and dispersions, and their estimated errors, are presented in Tables 1 and 2, and the rotation curves and stellar velocity dispersions for each position angle are shown in Figures 1a, 1c, and 1d.

The FWHM of the [O II] doublet was measured by fitting Gaussian profiles to the emission lines. To find the true velocity dispersion of the gas, we have to correct the measured FWHM for the instrumental profile and for the presence of the unresolved doublet. This last step cannot be done reliably, so we cannot discuss the gas velocity dispersion derived from the ESO spectra in any quantitative way.

2.2. Spectroscopic Observations at CTIO

To extend our coverage of the gas velocity field, two further spectra were taken at P.A. 52° in 1987 February with a GEC CCD camera on the RC spectrograph at the Cassegrain focus of the CTIO 4 m telescope. The wavelength range in this case was

TABLE 1
ABSORPTION-LINE MEASUREMENTS^a

r''	γ	v_{abs}	σ_{abs}
P.A. = 7°			
-19.2.....	...	2737 ± 32	...
-17.3.....	...	2760 ± 25	...
-15.4.....	...	2821 ± 85	...
-13.5.....	...	2813 ± 74	...
-11.5.....	0.63 ± 0.11	2723 ± 33	214 ± 17
-9.6.....	0.65 ± 0.08	2744 ± 22	206 ± 14
-7.7.....	0.85 ± 0.08	2740 ± 20	240 ± 11
-5.8.....	0.98 ± 0.07	2727 ± 22	240 ± 10
-3.8.....	0.97 ± 0.07	2754 ± 23	204 ± 10
-1.9.....	0.94 ± 0.05	2757 ± 18	226 ± 9
0.0.....	0.80 ± 0.04	2734 ± 15	251 ± 8
1.9.....	0.76 ± 0.04	2734 ± 15	242 ± 9
3.8.....	0.89 ± 0.06	2737 ± 17	224 ± 10
7.7.....	0.85 ± 0.07	2775 ± 21	208 ± 11
9.6.....	0.95 ± 0.09	2782 ± 23	230 ± 11
11.5.....	0.80 ± 0.09	2767 ± 32	244 ± 14
13.5.....	...	2762 ± 38	...
15.4.....	...	2683 ± 43	...
17.3.....	...	2641 ± 44	...
19.3.....	...	2664 ± 57	...
21.2.....	...	2677 ± 72	...
23.1.....	...	2687 ± 77	...
25.0.....	...	2681 ± 46	...
P.A. = 97°			
-13.5.....	0.67 ± 0.22	2622 ± 78	...
-11.5.....	0.80 ± 0.20	2719 ± 25	242 ± 16
-9.6.....	0.86 ± 0.16	2760 ± 35	223 ± 15
-7.7.....	0.91 ± 0.13	2750 ± 32	229 ± 15
-5.8.....	0.83 ± 0.10	2748 ± 25	239 ± 16
-3.8.....	0.90 ± 0.09	2776 ± 19	230 ± 14
-1.9.....	1.16 ± 0.08	2785 ± 15	238 ± 10
0.0.....	1.22 ± 0.08	2768 ± 15	243 ± 12
1.9.....	1.31 ± 0.07	2761 ± 13	230 ± 12
3.8.....	1.35 ± 0.07	2782 ± 16	224 ± 10
5.8.....	1.34 ± 0.09	2812 ± 21	212 ± 11
7.7.....	...	2814 ± 19	...
9.6.....	1.09 ± 0.10	2792 ± 27	257 ± 11
11.5.....	1.02 ± 0.11	2873 ± 28	239 ± 18
13.5.....	0.97 ± 0.13	...	216 ± 15
P.A. = 127°			
-7.7.....	0.67 ± 0.26	2850 ± 67	...
-5.8.....	0.53 ± 0.11	2797 ± 32	205 ± 15
-3.0.....	0.73 ± 0.09	2719 ± 27	227 ± 13
-1.9.....	0.81 ± 0.08	2724 ± 24	243 ± 13
0.0.....	0.80 ± 0.07	2723 ± 26	258 ± 12
1.9.....	0.83 ± 0.07	2780 ± 44	213 ± 15
5.8.....	0.67 ± 0.10	2780 ± 45	227 ± 17
7.7.....	0.82 ± 0.13	2789 ± 44	235 ± 21

^a ESO data

6500–7100 Å, with a spectral resolution of 2.2 Å and a spatial scale of 0".73 pixel⁻¹, and the exposure time for each spectrum was 1000 s. In contrast to our earlier ESO data, these new spectra (at H α /[N II]) also allow us to measure the gas velocity dispersion as a function of radius.

The positions of the H α λ 6562.8 and [N II] λ 6583.8 emission lines were measured directly from the reduced spectra using a centroid-finding algorithm from the IRAF reduction package (Valdes 1986). Velocities from these two lines, and from the two different spectra, generally agreed to within ± 15 km s⁻¹ and the mean rotation curve is plotted in Figure 1*b*. The FWHM of the [N II] emission lines was corrected for the instrumental profile, and Figure 1*b* also shows the resulting velocity dispersion profile of the gas. The results are listed in Table 3.

2.3. Spectroscopic Observations at the AAT

Since the original spectrum at P.A. 97° showed some evidence for minor-axis stellar rotation, a second spectrum at this position was taken at the 3.9 m Anglo-Australian Telescope (AAT) in 1988 March. The detector was the IPCS with wavelength range 4700–5700 Å, spectral resolution 1.2 Å and spatial scale 2".3 pixel⁻¹. Again, several K-giant stars were observed as templates, and

TABLE 2
EMISSION-LINE MEASUREMENTS^a

r''	v_{em}	r''	v_{em}
P.A. = 97°			
-36.5.....	2590	-4.5.....	2698
-34.6.....	2624	-1.9.....	2772
-32.6.....	2550	0.0.....	2851
-30.7.....	2601	2.1.....	2875
-28.5.....	2649	4.0.....	2947
-27.0.....	2668	5.9.....	2968
-25.0.....	2679	7.5.....	3001
-23.1.....	2653	9.5.....	3026
-21.0.....	2663	11.4.....	2976
-18.8.....	2618	13.5.....	3002
-17.3.....	2638	15.0.....	3059
-15.2.....	2582	17.2.....	2977
-13.1.....	2549	19.8.....	2976
-10.7.....	2603	23.0.....	2984
-8.5.....	2625	27.9.....	3100
-6.6.....	2659		
P.A. = 7°			
-9.3.....	2688	1.9.....	2823
-7.5.....	2723	3.9.....	2803
-6.6.....	2740	5.9.....	2826
-4.6.....	2745	8.0.....	2882
-2.0.....	2797	10.0.....	2892
0.0.....	2810		
P.A. = 127°			
-19.3.....	2676	0.0.....	2910
-17.3.....	2715	1.9.....	2952
-15.4.....	2685	3.9.....	3021
-13.5.....	2665	5.8.....	3050
-11.6.....	2687	7.7.....	3083
-9.6.....	2690	9.6.....	3075
-7.7.....	2749	11.6.....	3025
-5.8.....	2777	13.5.....	3010
-3.9.....	2800	15.4.....	2890
-1.9.....	2861		

^a ESO data

TABLE 3
EMISSION-LINE MEASUREMENTS^a

P.A. = 52°		
r''	v_{em}	σ_{em}
-6.9.....	2634 ± 13	...
-4.0.....	2657 ± 14	133 ± 15
-1.8.....	2691 ± 9	162 ± 8
-0.3.....	2780 ± 5	244 ± 14
0.4.....	2843 ± 20	240 ± 5
1.1.....	2860 ± 14	179 ± 16
2.6.....	2877 ± 12	152 ± 6
4.8.....	2912 ± 11	118 ± 9
7.7.....	2873 ± 26	103 ± 18

^a CTIO data

TABLE 4
ABSORPTION-LINE MEASUREMENTS^a.

P.A. = 97°			
r''	γ	v_{abs}	σ_{abs}
-29.1.....	...	2843 ± 67	...
-17.6.....	0.68 ± 0.12	2780 ± 22	227 ± 25
-9.6.....	0.82 ± 0.12	2677 ± 20	228 ± 20
-6.1.....	0.80 ± 0.11	2728 ± 20	189 ± 20
-3.8.....	0.89 ± 0.08	2753 ± 12	236 ± 15
-1.5.....	0.93 ± 0.13	2741 ± 12	258 ± 15
0.8.....	0.92 ± 0.06	2816 ± 12	232 ± 15
3.1.....	0.92 ± 0.06	2851 ± 12	266 ± 15
5.4.....	0.88 ± 0.10	2777 ± 17	243 ± 19
8.8.....	0.83 ± 0.11	2847 ± 20	232 ± 20
16.9.....	0.74 ± 0.14	2764 ± 26	222 ± 28
28.4.....	...	2817 ± 67	...

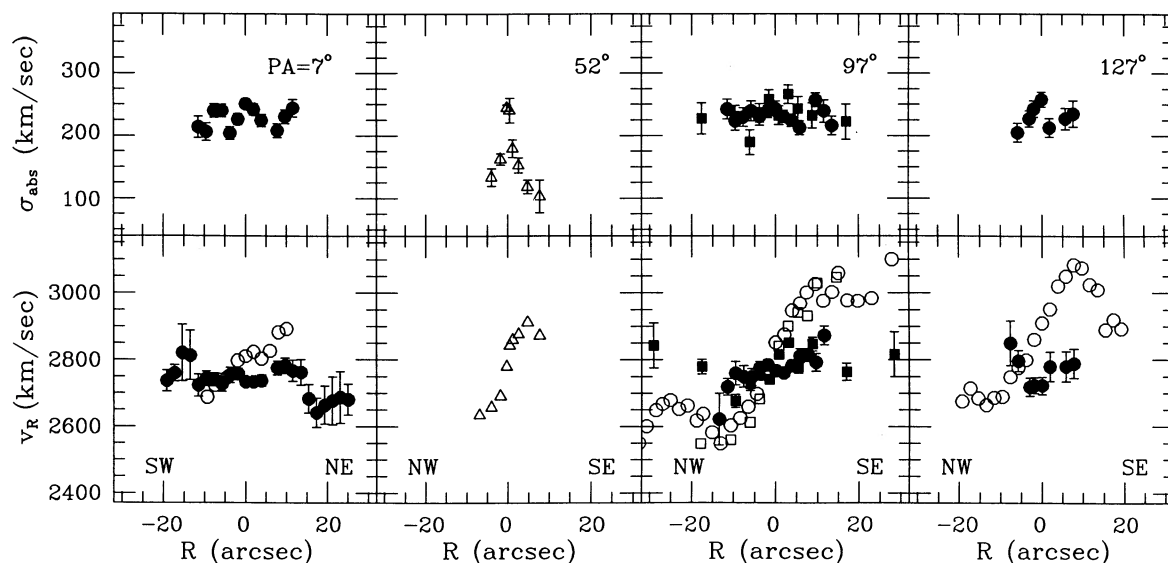
^a AAT data.

FIG. 1.—Radial velocity and velocity dispersion for NGC 5077 as a function of radius along four position angles. Filled symbols represent absorption-line measurements (stars) and open symbols emission-line observations (gas), while observations at ESO, CTIO, and the AAT are shown by circles, triangles, and squares, respectively. Velocity dispersion measurements at P.A. 52° are for gas, not stars.

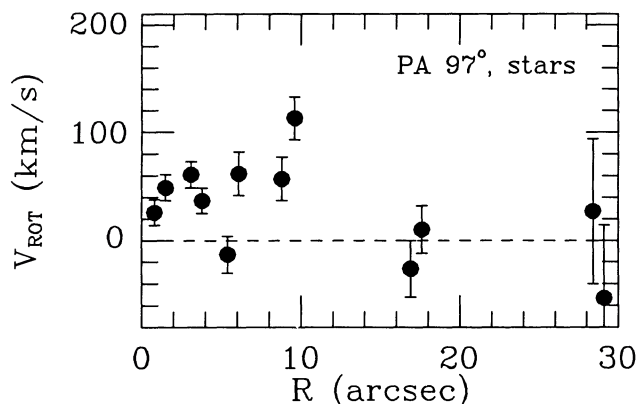


FIG. 2.—The stellar absorption-line measurements at P.A. 97° shown in more detail with an expanded velocity scale, and folded around the center

absorption-line velocities and velocity dispersions were measured by the Fourier quotient technique. The results are shown in Figure 1c and in more detail in Figure 2, where we have folded the velocities with respect to the center. The data are listed in Table 4. Gas velocities were measured by a Gaussian fit to the [O III] $\lambda 5007$ emission line. The results are given in Figure 1c and Table 5, and agree well with the values measured at ESO.

2.4. Imaging the Emission-Line Gas

Images of the ionized gas were taken with an RCA CCD at the Cassegrain focus of the ESO/MPI 2.2 m telescope at La Silla. We used two interference filters: a line + continuum filter with central wavelength 6646 Å and bandpass 78 Å, and a continuum filter with central wavelength 6480 Å and bandpass 70 Å. The CCD covered an area $3'.1 \times 2'.0$ on the sky, with a scale of $0''.363 \text{ pixel}^{-1}$. The seeing during these observations was $1''.0$ FWHM.

The CCD images were reduced in the standard way. While fringing at a level of 2%–3% was seen in the original frames, this was reduced to below 0.5% by a flat-field division. A more serious problem was the presence of background structure in the form of diagonal lines running across the image and visible at low light levels. This phenomenon (probably caused by a grounding problem in the CCD electronics) could not be removed effectively by flat-fielding and is present at a low level in the final data.

About six field stars in each frame were used to align the two images, and the alignment is accurate to 0.1 pixel ($0''.04$). The interpolation process used for alignments smaller than 1 pixel produces a slight broadening of the final image, so the profiles of stars in each image were measured and a Gaussian filter applied to ensure that the FWHM of images in each frame was identical (if this is not done, the final subtraction may produce spurious “emission” features). The stars were also used to check the flux scale, since the bandpass and transmission of the two filters are not identical. Magnitudes of several stars in each frame were measured and an adjustment made so that the mean stellar magnitude was the same in each of the two frames. The continuum image was then subtracted from the line + continuum image to give the distribution of line emitting gas seen in Figure 3 (Plate 1). The two images were also analyzed using the GRASP profile-fitting package developed by M. Cawson and R. Jędrzejewski (see, e.g., Jędrzejewski 1987).

2.5. Imaging the Stellar Continuum

CCD images in *B* and *I* were kindly obtained for us at the ESO/Danish 1.5 m telescope by G. Galletta. The seeing was $1''.5$ FWHM and the images show that little dust is associated with the extended gas structure.

The surface brightness profiles of the narrow-band continuum and line + continuum images, and of the broad-band *B* image, are shown in Figure 4. The *B* luminosity profile closely follows an $R^{1/4}$ law except in the very inner regions where seeing affects the data.

TABLE 5
EMISSION-LINE MEASUREMENTS^a

r''	P.A. = 97°	
	v_{em}	σ_{em}
−17.9	2548	38
−10.7	2559	61
−6.1	2612	78
−3.8	2682	96
−1.5	2780	151
0.8	2841	157
3.1	2900	116
5.4	2941	91
7.7	2931	82
10.0	3029	76
14.6	3046	35

^a AAT data.

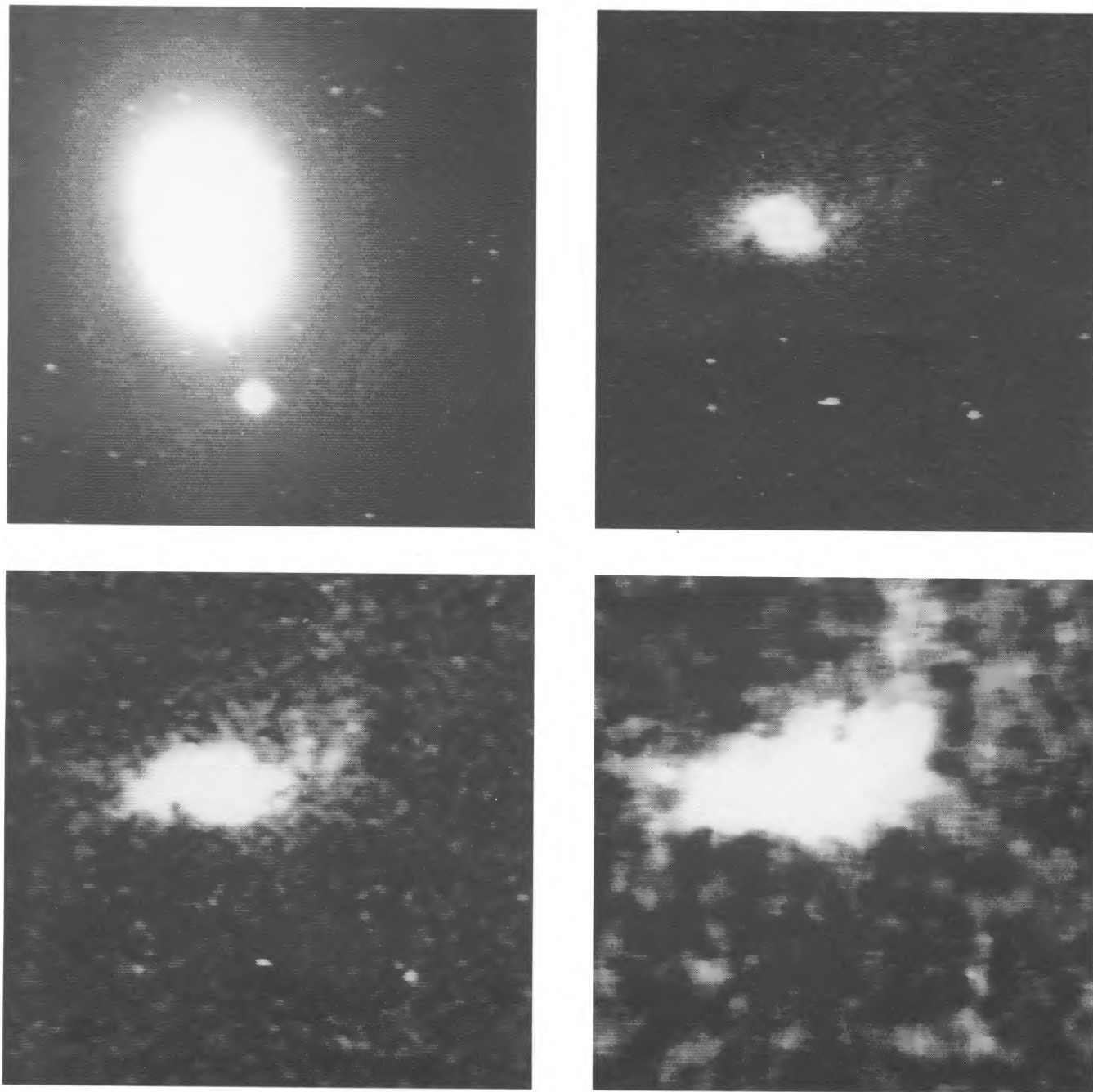


FIG. 3.—Distribution of emission-line gas in NGC 5077, as derived from subtraction of the CCD continuum image from the line + continuum image. Each of the four pictures covers $1' \times 1'$. The top left-hand picture shows a continuum image of NGC 5077, while the three remaining images show the emission-line gas. The two lower images have been median-filtered to show low-level structure in the outer regions of the disk. North is to the top and east is to the left.

BERTOLA et al. (see 373, 373)

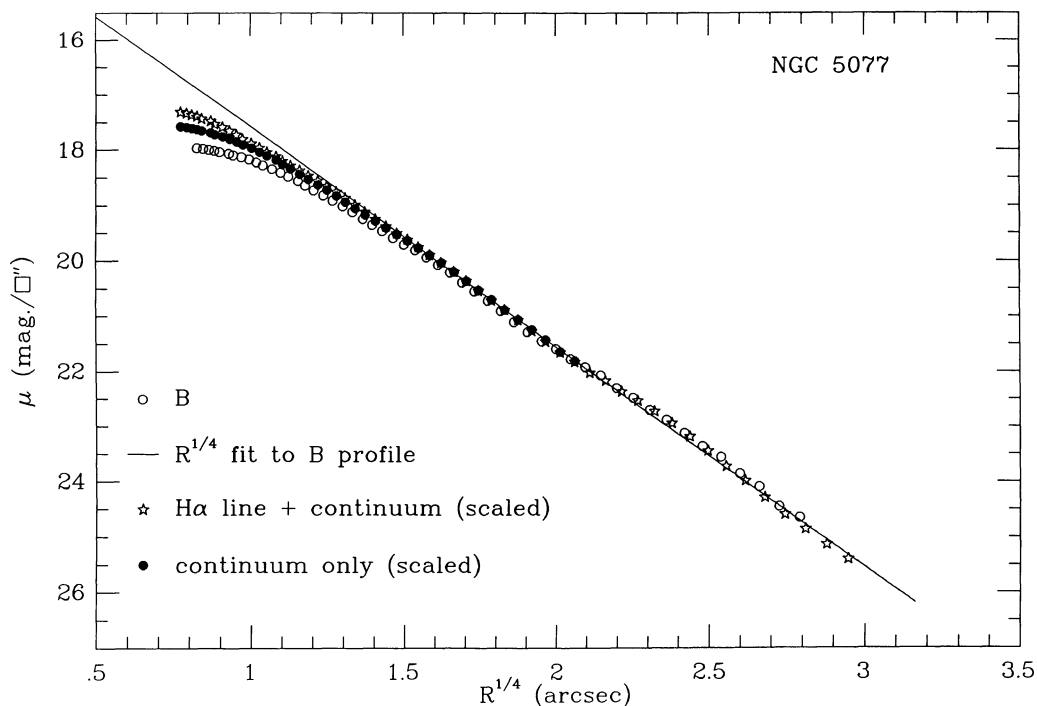


FIG. 4. Surface brightness profiles along the major axis of NGC 5077. Filled circles are from broad-band B photometry, and open circles show the continuum emission, scaled to match the B magnitudes. Five-pointed stars show the sum of the continuum emission and the $H\alpha$ line emission, again scaled. The solid line is the best fit of a de Vaucouleurs $R^{1/4}$ law to the B profile.

The best fit gives $R_e = 19''$ and $\mu_e = 22.2$ mag arcsec $^{-2}$ (where R_e is the radius of the circular isophote containing half the total light, and μ_e is the surface brightness within an aperture of radius R_e).

Figure 5a shows the ellipticity profile $\epsilon(R)$, and Figure 5b shows the position angle $\Phi(R)$ of the apparent major axis as function of projected radius R along the major axis. The isophotes show little variation in ellipticity, becoming only slightly rounder at large radii, and there is no significant isophotal twisting. Figure 5c shows the parameter $B_4(R)$ ($\cos 4\theta$), which measures the deviation of the isophote shape from a pure ellipse (Jedrzejewski 1987). B_4 is negative over a large range in radius, showing that the stellar isophotes are slightly box-shaped.

2.6. H I Observations

Observations at Parkes in 1988 May detected neutral hydrogen in emission from NGC 5077 (Sadler & Whiteoak 1991). The H I linewidth is ~ 500 km s $^{-1}$ FWZI and the total mass of H I associated with the galaxy is estimated as $3 \times 10^9 M_\odot$. Further observations with the VLA, to measure the H I velocity field in detail, are in progress.

2.7. Results

The main results from the above observations are as follows.

1. The luminosity profile of NGC 5077 is well-fitted by an $R^{1/4}$ law with a half-light radius R_e of $19''$ and a core radius less than $1''$. Thus NGC 5077 appears to be a typical elliptical galaxy in spite of the presence of the gas disk.
2. The overall gas distribution is markedly elongated along the apparent minor axis of the galaxy and extends to $\sim 30'' \times 15''$. On the west side, the gas structure bends toward the north, and there is a faint filament roughly parallel to the stellar major axis. This structure may be a warp or an outer arm lying in the same plane as the disk.
3. The gas twists strongly in the inner regions, and the region of most intense emission is significantly misaligned with the photometric axes of the stellar surface brightness distribution.
4. The gas rotation curve rises slowly, reaching its maximum value of 250 km s $^{-1}$ at $\sim 10''$ radius.
5. In the outer parts of the galaxy there is no measurable stellar rotation at any of the three position angles observed ($V_{\max} < 15$ km s $^{-1}$). However, the data at P.A. 97° suggest that NGC 5077 may have a rotating stellar core with a radius of $\sim 10''$ and a maximum rotation velocity of ~ 60 km s $^{-1}$ (see Fig. 2). If so, this galaxy belongs to the small but growing class of ellipticals recognized as having dynamical substructure (Franx & Illingworth 1988; Jedrzejewski & Schechter 1988; Bender 1988; Illingworth & Franx 1989).
6. The stellar velocity dispersion remains roughly constant at ~ 230 km s $^{-1}$ along each position angle, though the data are rather noisy.

3. SPHERICAL AND AXISYMMETRIC MASS MODELS

If we know the intrinsic shape of a galaxy, then measuring the velocity field of a disk of cold gas orbiting the galaxy allows us to set strong constraints on the mass distribution. We first consider the simplest case of gas in a circular disk in a spherical potential,

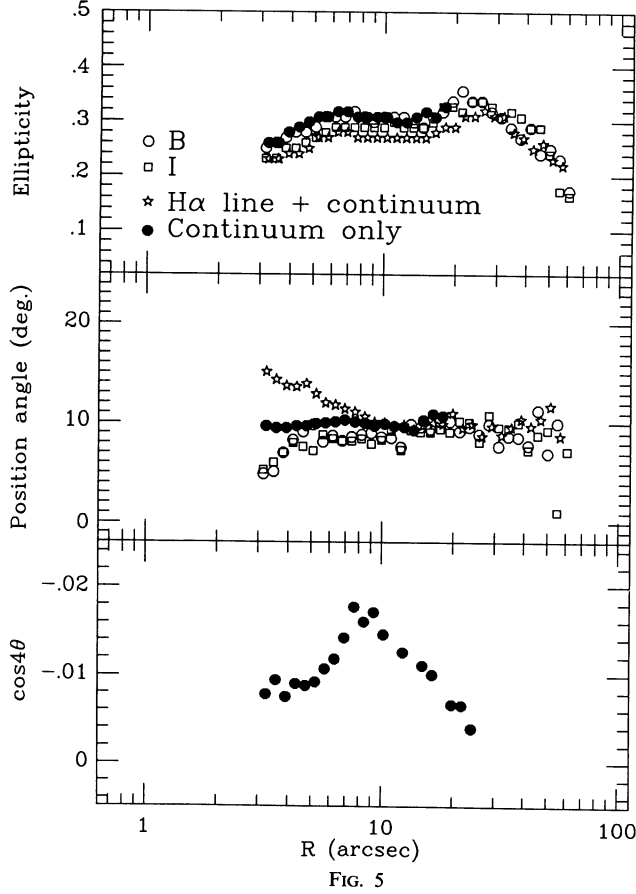


FIG. 5

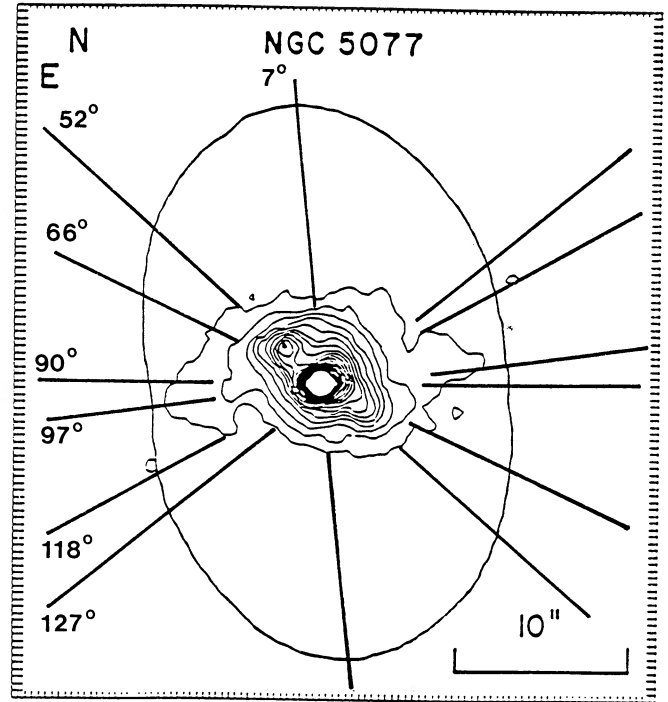


FIG. 6

FIG. 5.—Ellipticity ϵ , major axis position angle Φ , and shape indicator B_4 , as functions of the radius R along the major axis of NGC 5077. Symbols are the same as Fig. 4.

FIG. 6.—The seven position angles for radial velocity measurements, superposed on a contour map of the ionized gas. Solid lines show our own observations and the three position angles studied by DBB. The outermost contour is an isophote of the underlying stellar galaxy.

then study axisymmetric models with the gas on circular orbits in the equatorial plane. None of these simple models gives a satisfactory description of the observed morphology and kinematics of NGC 5077, and we discuss more sophisticated models in §§ 4 and 5.

3.1. Gas Velocity Field

We combined the gas velocities derived from our own data (P.A. 7° , 52° , 97° , and 127°) with those measured by DBB (P.A. 66° , 90° , and 118°). Figure 6 shows these seven slit positions, superposed on a contour map of the emission from the gas disk. For the subsequent modeling, it is useful to fit the gas velocities with a simple functional form. We assume that the gas is on circular orbits in a plane and has a rotation curve given by

$$v_c(r) = \frac{Ar}{(r^2 + c_0^2)^{p/2}}, \quad (1)$$

where A , c_0 , and p are parameters, and r is the radius. This rotation curve rises linearly in the center, and is proportional to $r^{(1-p)}$ at larger r . For $p = 1$ the rotation curve is asymptotically flat, while for $p = 3/2$ the system has a finite total mass. Hence, for applications to galaxies, we expect $1 \leq p \leq 3/2$.

The observed radial velocity at a position (R, Ψ) on the plane of the sky is related to the circular velocity $v_c(r)$ by the equations given in, e.g., van der Kruit & Allen (1978). For the rotation curve (1) we find explicitly

$$v_{\text{mod}}(R, \Psi) = v_{\text{sys}} + \frac{AR \cos(\Psi - \Psi_0) \sin \theta \cos^p \theta}{\{(R^2[\sin^2(\Psi - \Psi_0) + \cos^2 \theta \cos^2(\Psi - \Psi_0)] + c_0^2 \cos^2 \theta)^{p/2}}, \quad (2)$$

where θ is the inclination of the disk (with $\theta = 0$ for a face-on disk), Ψ_0 is the position angle of the line of nodes and v_{sys} is the systematic velocity. We determined A , c_0 , p , Ψ_0 , and θ simultaneously by minimizing the residuals $\Delta v = v_{\text{obs}} - v_{\text{mod}}$, where $v_{\text{mod}}(A, c_0, p, \Psi_0, \theta, r, \Psi)$ is the velocity predicted by equation (2) at radius R and position angle Ψ on the sky, and $v_{\text{obs}}(R, \Psi)$ is the observed velocity at that position.

We used a nonlinear least-squares (Levenberg-Marquardt) algorithm to fit the model to the observed velocity field. To eliminate

TABLE 6
FITS TO OBSERVED VELOCITY FIELD

Parameter	Circular fit	Gas \perp Shortest Axis	Gas \perp Longest Axis
A (km s $^{-1}$)	503	360	333
c_0 (arcsec)	7.35	1.43	2.68
p	1.12	1.12	1.12
ϕ	-13°	-39°
θ	52°	52°	52°
rms (km s $^{-1}$)	20	37	43
b/a	0.51	0.92
c/a	0.44	0.54

any systematic velocity offsets between different sets of observations, v_{sys} was determined separately for each position angle. This was done by first fitting the entire data set with A , c_0 , p , Ψ_0 , θ , and v_{sys} as free parameters, but v_{sys} having the same value for all data points. We then fitted the data at each position angle separately, keeping the values of A , c_0 , p , Ψ_0 , and θ fixed and varying only v_{sys} . Finally, we fitted the whole data set once again with A , c_0 , p , θ , and Ψ_0 as free parameters, using a fixed value of v_{sys} for each position angle. The final data set contained 114 velocity measurements.

The best fit to the gas velocity field in NGC 5077 is given in Table 6. The rms deviation from the circular fit is consistent with the observational errors in the velocity measurements (25–40 km s $^{-1}$).

In practice, since p measures the slope of the rotation curve in the “flat” outer regions outside $10''$ – $12''$, it is constrained mainly by the data at P.A. 97° . Most of the data points at other position angles lie on the steeply rising part of the rotation curve and do not constrain p . The inclination angle, θ , is also poorly determined by the circular fit. The observed axis ratio of the gas disk, assuming it is intrinsically circular, gives $\theta \sim 60^\circ$, but the best fit to the observed velocity field has $\theta \sim 45^\circ$, and in practice, θ could reasonably lie anywhere between 45° and 60° . Regardless of the adopted values of p and θ , the position angle of the line of nodes, Ψ_0 , is well determined and lies close to P.A. 76° . This value does not appear to vary much with radius over the range covered by our data. It follows that Ψ_0 differs from the position angle of the apparent minor axis of the surface brightness distribution of the stellar light by 23° , with an estimated uncertainty of about $\pm 5^\circ$.

Because the model circular velocity field fits the observations to within the accuracy of the observations, it is unlikely that there is substantial *large-scale* noncircular motion of the gas (such as inflow or outflow). However, the emission-line velocity dispersions observed well outside the nucleus are 50–100 km s $^{-1}$, whereas the dispersion expected from thermal motions of the gas ($T \sim 10^4$ K) is only 10–15 km s $^{-1}$. Thus there is probably small-scale turbulence throughout the gas disk.

To summarize, the observed radial velocities in NGC 5077 are consistent with the gas lying in a circular disk with its rotation axis misaligned by $23^\circ \pm 5^\circ$ from the apparent major axis of the stellar light distribution. Since with the present observational uncertainties the gas velocity field shows no evidence for shearing or warping (for example, when we fit a circular velocity field separately to the inner and outer parts of the disk we find the same line of nodes to within the errors of the data), we will assume for now that the gas has settled onto stable orbits in the potential of the galaxy.

In the initial fit of a circular velocity field, we found that the observations at P.A. 127° gave unusually large residuals, and that gas velocities observed on the southeast side of the galaxy at this position were much higher than predicted by the circular fit. A second spectrum was taken along P.A. 127° at the AAT in 1989 January, with spectral resolution 1.2 \AA in the range 3500–4500 \AA . This spectrum suggests there may be a second, higher velocity component at $5''$ – $15''$ radius along P.A. 127° . Our CCD images show a small companion galaxy to the southeast of NGC 5077, close to this position angle and $\sim 46''$ away. Because the [O II] $\lambda 3727$ line is a doublet, the effects of velocity blending are complex and for now we have removed the affected points from the velocity fit. High-resolution observations of an unblended line such as [O III] $\lambda 5007$ would be valuable in tracing the high-velocity component.

3.2. Spherical Model

In a spherical potential, the rotation curve (1) corresponds to a mass distribution $M(r)$ given by

$$M(r) = \frac{1}{G} r v_c^2(r) = \frac{A^2 r^3}{G(r^2 + c_0^2)^p}, \quad (3)$$

where G is the gravitational constant. The corresponding density $\rho(r)$ is given by

$$\rho(r) = \frac{1}{4\pi G r^2} \frac{d}{dr} [r v_c^2(r)] = \frac{A^2 [(3 - 2p)r^2 + 3c_0^2]}{4\pi G (r^2 + c_0^2)^{p+1}}. \quad (4)$$

To derive a density profile $\rho(r)$ directly from an observed rotation curve, we would have to differentiate $r v_c^2(r)$ with respect to r by numerical means, which introduces unwanted errors. For that reason we have fitted the observed rotational velocities with a smooth function which allows us to calculate the corresponding density profile analytically.

Figure 7 shows the profile (4) for the values of A , c_0 , and p for which expression (1) best fits the observed radial velocities. The spatial profile of the B light in NGC 5077 is also shown for comparison. This was obtained by using the values tabulated by Young (1976) for a spherical galaxy obeying the $R^{1/4}$ law, which, as we have seen, is a good approximation to the luminosity profile of NGC 5077. In the central regions, the density profile in Figure 7 is substantially flatter than the light profile. At larger radii the profiles

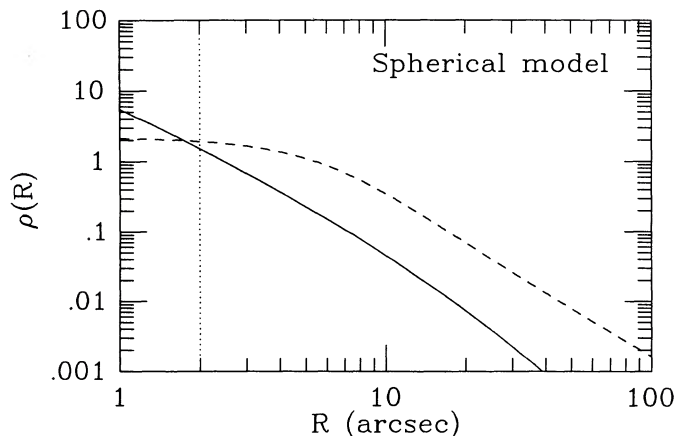


FIG. 7.—Density profile of the spherical mass model which corresponds to the rotation curve of NGC 5077 (*dashed line*) and luminosity density distribution derived from the best fitting de Vaucouleurs profile (*solid line*). The region to the left of the vertical (*dotted*) line is affected by seeing in our observations.

have nearly the same slope. A formal consequence of this is that the mass-to-light ratio, M/L , is ~ 7.5 in the outer regions of the galaxy and drops to 1 or less in the innermost few arcseconds.

This apparent variation in M/L arises because c_0 is large, i.e., the fitted rotation curve rises linearly over a large range in radius. We investigated the effects of seeing on model rotation curves of the form (1) with different values of c_0 , and found that “observed” values of c_0 are indistinguishable from the true ones as long as c_0 is larger than about twice the radius of the seeing disk. For our observations the seeing was 1.5 FWHM, and we find c_0 between 8” and 10”. Thus the apparent central drop in M/L is not an artifact caused by seeing.

The velocity dispersion of the gas in NGC 5077 rises sharply in the center (see Fig. 1*b*), and this will also lower the observed rotation velocities. The size of this effect can be estimated from the equation for asymmetric drift (Oort 1965), and we find that there should be no appreciable effect on rotational velocities beyond $\sim 2''$ – $3''$ from the center. Thus the circular fit to the rotation curve implies that M/L varies from 1 to 7 over the region from 2”–10” where no limitation in resolution should be present.

If we assume that the stellar velocity dispersion is constant at 250 km s $^{-1}$ out to about R_e , which is consistent with what we observe, we can also derive a global value of M/L from the stars. Following Binney (1982), we have for a spherical de Vaucouleurs galaxy,

$$\left\langle \frac{M}{L_B} \right\rangle = \frac{0.047\sigma^2}{I_e R_e}, \quad (5)$$

where R_e is the half-light radius in kiloparsecs, I_e is the surface brightness at R_e in units of L_\odot pc $^{-2}$ and σ is the stellar velocity dispersion in km s $^{-1}$. This gives $\langle M/L_B \rangle = 7.2$ in solar units, in agreement with the value derived from the outer parts of the gas rotation curve.

3.3. Axisymmetric Models

It is unlikely that the mass distribution of NGC 5077 is spherical, since even in projection it is an E3 galaxy. We therefore relax the assumption of spherical symmetry, and estimate the effect on the measured value of M/L .

If NGC 5077 is axisymmetric, with the gas on circular orbits in the equatorial plane, then its shape must be prolate rather than oblate since the gas is observed to be elongated along the minor axis of the galaxy rather than the major axis. By contrast with the spherical case, for an axisymmetric galaxy we must make some assumptions about the density stratification within the galaxy before we can derive the mass distribution from an observed rotation curve (e.g., Burbidge, Burbidge, & Prendergast 1959). Accordingly, we made several prolate models using the families 1 and 2 of the potential-density pairs described in detail by de Zeeuw & Lynden-Bell (1988) and de Zeeuw & Pfenniger (1988, hereafter dZP), for which the rotation curve—again taken to be of the form given in equation (1)—determines the density distribution. We were able to find models of this kind with projected ellipticity profiles which matched those observed in NGC 5077, but they still had large cores of constant density which imply a central drop in M/L in the same way as found for the spherical model.

All prolate models with gas on the equatorial circular orbits have a crucial defect. The line of zero velocity should always lie along the observed major axis of the light distribution, but in NGC 5077 the zero-velocity line is 23° from the apparent major axis. There is no significant twisting, either of the stellar isophotes or of the kinematic axes, which could produce such a shift. Either the galaxy is not axisymmetric but triaxial, or the gas is in a warped polar disk. We will investigate these alternatives in the following sections.

4. TRIAXIAL MODELS

It is generally thought that giant elliptical galaxies are triaxial in shape and rotate slowly (e.g., Binney 1978; Davies 1987). Both our surface photometry and the observed lack of stellar rotation outside the core suggest that NGC 5077 is a typical elliptical galaxy in spite of its gas disk.

Triaxiality complicates the interpretation of observed gas velocities in two ways. The simple closed orbits on which cold gas

moves are roughly elliptic, rather than circular, and the velocity changes as gas moves around the orbit. Deprojecting the galaxy to find its intrinsic shape is more difficult, since there are now two axis ratios and two viewing angles.

We will first look at constraints on the intrinsic shape given by the morphology and kinematics of the stars, then investigate the gas velocity field in detail. We shall see that the position angle difference between the apparent major axis of the stellar light distribution and the line of zero velocity of the gas disk can be ascribed to projection effects and sets further constraints on the intrinsic shape. Finally, we calculate gas velocity fields of triaxial mass models of the proper shape and show that some of these are consistent with the observed velocities even though M/L remains constant with radius.

4.1. Morphology and Kinematics of the Stars

If the light distribution in a galaxy is stratified on similar, concentric ellipsoids with axis ratios b/a and c/a and the galaxy is observed from an arbitrary direction specified by two viewing angles θ and ϕ (as defined by Binney 1985), then the isophotes of the projected surface brightness distribution are exact ellipses with a fixed axis ratio and a fixed direction of the apparent major axis, i.e., the observed ellipticity $\epsilon(R)$ and position angle $\Phi(R)$ will be constant with radius for any direction of viewing (Contopoulos 1956; Stark 1977; Kondrat'ev & Ozernoy 1979; Binney 1985).

In NGC 5077, ϵ and Φ vary little with radius, and the isophotes are nearly elliptical. To first order we may assume that the light is stratified on similar ellipsoids. The observed value of $\epsilon \sim 0.3$ gives one constraint on the viewing angles and the axis ratios, and an explicit relation between $\epsilon = \epsilon(b/a, c/a, \theta, \phi)$ can be found (Binney 1985).

An observed lack of isophotal twisting does not necessarily rule out a triaxial galaxy with varying $\epsilon(R)$, or with isophotes that are not exact ellipses. Franx (1988a) established the existence of a large class of light distributions in which ϵ varies with R and the isophotes deviate from ellipses, yet there is no variation in Φ for an arbitrary direction of observation. This class includes the large family of triaxial models described by dZP. Hence when $\Phi(R)$ is observed to be constant—as in the case of NGC 5077—this does not necessarily imply that the galaxy is axisymmetric, or triaxial observed along one of its principal planes. It is equally likely that the light distribution in the galaxy is close to the general form discussed by Franx, and is viewed from an arbitrary direction. As a result, the observed constancy of $\Phi(R)$, and the small variation in $\epsilon(R)$ which we observe in NGC 5077 do not further constrain the intrinsic shape of the galaxy or put limits on the direction of viewing.

The absence of any observed gradient in the stellar velocity field outside the core implies one of three alternatives:

1. The galaxy has a nonrotating triaxial figure, and the stars do not stream within the figure. The limiting cases of an oblate or prolate figure are not ruled out.
2. The galaxy is triaxial or prolate, and we happen to look directly along the rotation axis of the figure, which is assumed to be the shortest axis.
3. The stars are streaming in a direction opposite to that of the figure rotation and with exactly the same speed.

We can reject the third alternative, since elliptical galaxies are strongly centrally concentrated and counter-streaming cannot balance the figure rotation over a large region. In general, one expects nonzero mean stellar velocities at most radii, as in the triaxial model constructed by Vietri (1988), which has counter-streaming in the inner few core radii. To decide between the first two possibilities we need more information, which can be provided by the morphology and kinematics of the gas in NGC 5077 as discussed below.

The core region of NGC 5077 may be kinematically distinct from the rest of the galaxy. The nonzero mean stellar velocities could arise from streaming within the core, or from a separate component such as a rapidly rotating disk (Franx & Illingworth 1988). Higher resolution observations of the stellar absorption lines would be very useful.

4.2. Morphology of the Gas

Consider the second of the two remaining alternatives for the structure of NGC 5077 mentioned in § 4.1. In a rotating triaxial galaxy, the stable configurations for gas are a disk in the equatorial plane with the gas on roughly elliptic orbits or a warped configuration along the minor axis with the gas on one of the two branches of the anomalous orbit family (Heisler, Merritt, & Schwarzschild 1982; Magnenat 1982).

In NGC 5077 has a rotating figure, and we observe it nearly exactly along the rotation axis, then the gas must be in a disk tilted by at least $\sim 30^\circ$ with respect to the plane perpendicular to the longest axis (since the observed axis ratio of the gas disk is ~ 0.5). Since, by assumption, the gas is in a stable configuration, it must be on the anomalous orbit family. The gas disk should appear symmetric with respect to the observed minor axis of the isophotes, but it is clear from Figures 3 and 6 that this is not the case. In addition, one would expect the line of nodes of the gas velocity field to be exactly along the minor axis of the isophotes and we have seen in § 3.1 that this is not the case either. Therefore we rule out the possibility of a rotating system viewed along the stellar rotation axis and assume from now on that NGC 5077 has a *nonrotating* triaxial figure.

4.3. Determination of Viewing Angles and Axis Ratios

A stable configuration of cold gas in a nonrotating triaxial galaxy can only be a ring or a disk in one of two principal planes, either perpendicular to the longest axis of the figure or perpendicular to the shortest axis (Tohline, Simonson, & Caldwell 1982; Merritt & de Zeeuw 1983). In either case, the gas in the disk is on roughly elliptic closed orbits and the orbits become nearly circular beyond a few core radii.

If the gas in NGC 5077 is cold, the preceding arguments imply that the observed radial velocity of the gas in the outer parts of the galaxy will be zero along the direction of the projected shortest axis or the projected longest axis of the stellar figure. For a triaxial galaxy, these directions generally differ from the position angle of the major axis of the projected light distribution (Contopoulos 1956; Kondrat'ev & Ozernoy 1979; Binney 1985; dZF).

For definiteness, we assume that the gas is in the (x, y) -plane of a triaxial galaxy with a luminosity density distribution given by

$$v(x, y, z) = v(m^2), \quad m^2 = \frac{x^2}{a^2} + \frac{y^2}{b^2} + \frac{z^2}{c^2}. \quad (6)$$

We choose the x and y directions by requiring $a \geq b$. The gas orbits are then elongated along the shorter of the two axes in the (x, y) -plane, as required by the equations of motion (e.g., dZF). The z -axis is the *shortest* axis of the system for $a \geq b \geq c \geq 0$, and the *longest* axis for $c \geq a \geq b \geq 0$. For $a \geq c \geq b \geq 0$ the z -axis is the intermediate axis, but the closed orbits in the plane perpendicular to this axis are unstable (Heiligman & Schwarzschild 1979) and gas cannot settle there, so we will consider only the first two cases.

We define our viewing angles θ and ϕ following Binney's (1985) convention, so that θ is the inclination angle of the disk (with $\theta = 0$ for a face-on disk), and ϕ is an azimuthal angle in the plane of the disk. The direction of zero velocity of the gas at large radii is normal to the gas disk, along the projected z -axis. The major axis of the projected surface brightness of the galaxy will have a position angle Θ_* with respect to the projected z -axis. This is the misalignment angle between the rotation axis of the gas and the apparent major axis of the stellar light and is observed to be $23^\circ \pm 5^\circ$ in NGC 5077.

Θ_* is a function of b/a , c/a , θ , and ϕ , but is independent of the luminosity profile $v(m^2)$ (Binney 1985). It follows that the observed value of Θ_* constrains the viewing angles and axis ratios in a way that is independent of the constraint provided by the observed ellipticity ϵ (van Albada, Kotanyi, & Schwarzschild 1982).

As shown by dZF, the relations $\Theta_* = \Theta_*(b/a, c/a, \theta, \phi)$ and $\epsilon = \epsilon(b/a, c/a, \theta, \phi)$ can be inverted to give b/a and c/a explicitly as functions of θ , ϕ , ϵ and Θ_* . The resulting expressions are given in Appendix A of their paper. Thus, for each pair of assumed viewing angles, we can derive values of b/a and c/a consistent with the observed values of ϵ and Θ_* . As above, we accept these as a physical solution only if

$$a \geq b \geq c \geq 0, \quad \text{or} \quad c \geq a \geq b \geq 0. \quad (7)$$

Figure 8 shows the (θ, ϕ) -plane, with the regions of possible viewing angles allowed by the observed values of ϵ and Θ_* . By symmetry, we can restrict our attention to the ranges $-90^\circ \leq \phi \leq 90^\circ$ and $0^\circ \leq \theta \leq 90^\circ$ for the two viewing angles. For the case at hand it turns out that there are no physical solutions with $0^\circ \leq \phi \leq 90^\circ$, so Figure 8 shows only the ranges $-90^\circ \leq \phi \leq 0^\circ$ and $0^\circ \leq \theta \leq 90^\circ$. The two allowed regions—one for each of the two possibilities given in equation (7)—are bounded by curves which correspond to equality signs in equation (7). Inspection of equation (A8) of dZF reveals that in this case $\tan \phi$ can be found as the solution of a linear or quadratic equation with coefficients that depend on θ , so the boundary curves can be calculated easily. Since elliptical galaxies are no flatter than E7 (Binney & de Vaucouleurs 1981), we have also plotted the curves for which the ratio of shortest to longest axis is equal to 0.3 (i.e., $c/a = 0.3$ in the first case of equation (7), and $b/c = 0.3$ in the second case). These can be derived from equations (A8) of dZF in a similar manner. This restriction further limits the range of possible viewing angles to the hatched area. The boundary $b = c$ of the upper region corresponds to solutions where the gas disk orbits one of the short axes of a prolate system, while the boundary $c = a$ of the lower hatched region gives the solution for a polar gas disk in an oblate galaxy.

For each set of two viewing angles θ and ϕ , the constraints provided by the ellipticity ϵ and the misalignment angle Θ_* fix the axis ratios of the corresponding model. Hence the two allowed regions in Figure 8 correspond to two ranges of possible axis ratios. These are the two triangular regions shown in Figure 9a. It turns out that for each of these the boundaries are set by the observed ellipticity of the galaxy and the choice of 0.3 as a lower limit to the ratio of the shortest and the longest axis. The extra constraint given by the observed value of Θ_* does not limit the range of allowed axis ratios further, but it reduces the range of viewing angles for which a model with given axis ratios has an observed ellipticity of 0.3 to just one direction.

An extra constraint on the viewing angles can be found from the morphology of the gas. Since the gas orbits become nearly circular at large radii, the apparent axis ratio of the gas disk is directly related to the inclination angle θ . The observed axis ratio of

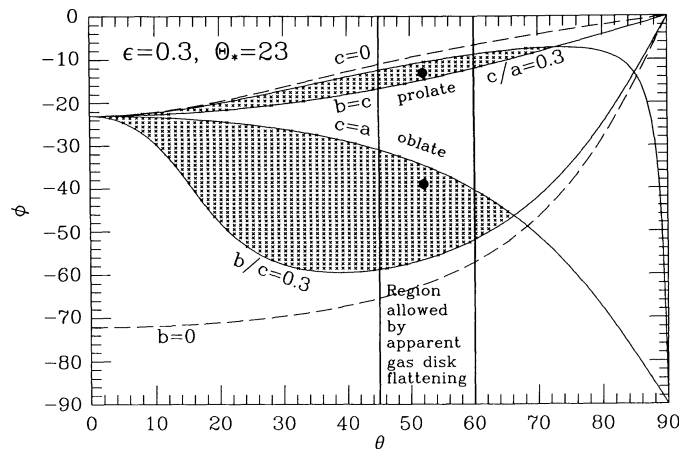


FIG. 8.—Plane of possible viewing angles (θ, ϕ) for a triaxial model of NGC 5077, assuming that the gas disk lies in the plane perpendicular to either the shortest or the longest axis. The hatched areas show the two regions allowed by the observed values of ϵ and Θ_* . The bounding curves correspond to equality signs in eq. (7). The range of θ consistent with the observed flattening of the gas disk is bounded by the two vertical solid lines. The two solid dots show the location of the triaxial models in Table 6 whose rotation curves are plotted in Fig. 10.

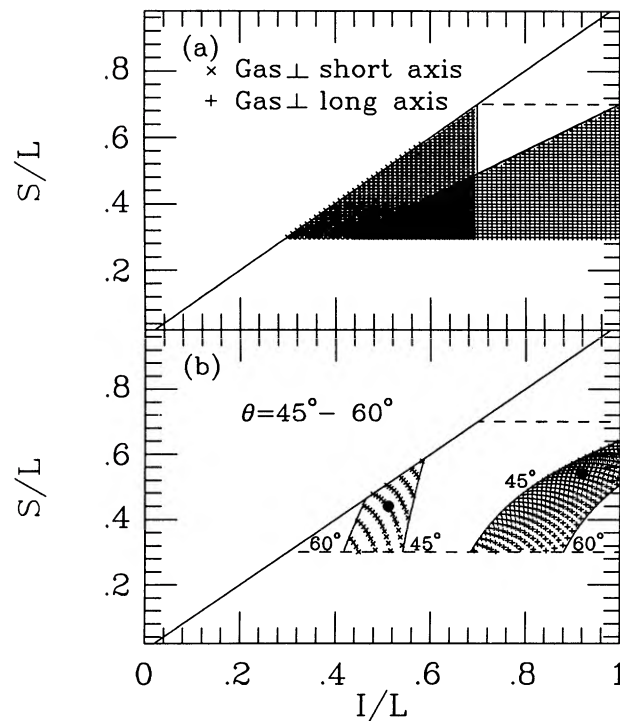


FIG. 9.—(a) Plane of axis ratios: S/L is the ratio of the short and the long axis, and I/L is the ratio of the intermediate and the long axis. The regions of values for I/L and S/L allowed by the observed values of ϵ and Θ_* are hatched. Crosses correspond to models with gas in the plane perpendicular to the short axis, and plus signs to models with gas in the plane perpendicular to the long axis. (b) Same plane, but now with only those values of S/L and I/L consistent with the additional constraint that θ must lie between 45° and 60° . As in Fig. 8, the two solid dots show the location of the triaxial models in Table 6.

the gas disk is between 0.4 and 0.6 but there is some uncertainty in using this to derive θ , both because we do not know how the emissivity of the gas varies with position and because the disk itself seems to possess substructure. Thus we do not know whether it is intrinsically circular, slightly elliptical, or even somewhat warped at the largest radius we can observe.

For the same reason, the observed central twisting of the disk isophotes cannot be used to provide further constraints on its intrinsic shape. Still, it is reasonable to assume that θ lies between 45° and 60° (see § 3.1). Inspection of Figure 8 shows that these bounding values of θ intersect the hatched areas, so that the observed flattening of the gas disk is consistent with the independent constraints provided by ϵ and Θ_* . The corresponding remaining values of b/a and c/a are shown in Figure 9b. Clearly exactly oblate or prolate configurations with the gas in elliptic orbits over the pole are not ruled out, but these polar orbits are marginally unstable and gas is unlikely to settle onto them (see also § 5). Slight triaxiality of the potential will, however, stabilize the gas in these orbits.

4.4. Gas Velocity Field

From Figures 8 and 9, it follows that the constraints which we have imposed still leave us with a range of possible viewing angles and axis ratios. For any of the allowed configurations, we would like to use the observed velocity measurements to determine the gravitational potential of the galaxy, and hence the density and the run of M/L with radius. This can be done if we assume that the gas is on simple closed orbits, but only if we make some further assumptions about the stratification of density in the model, just as was necessary for axisymmetric models (§ 3.3). In order to avoid numerical orbit calculations, we use models with a potential of Stäckel form. The simple closed orbits in such a potential are confocal ellipses, and the gas velocities can be given in analytic form. This has the advantage that many models can be studied, so that we can fit them to the observations by optimizing various parameters. We use the set of triaxial Stäckel models described in some detail in Appendix B of dZF. Their axisymmetric limiting cases have rotation curves identical to those given by equation (1). The models are specified by the two central axis ratios and a choice of A , p , and c_0 . Their density distributions are not stratified exactly on similar concentric ellipsoids, and become less flattened at larger radii. The contours of constant surface density (isophotes) are approximately elliptic in projection. The ellipticity varies with radius, but the position angle of the apparent major axis is constant, in agreement with the general result of Franx (1988a).

For a consistent treatment, one should repeat the intrinsic shape analysis of § 4.3 for the above Stäckel models. This can be done in a similar way (see dZF), but since the isophotes are nearly elliptic, and ϵ varies only slowly, one may simply use the values for b/a and c/a found in § 4.3 as the central axis ratios for the Stäckel model.

In principle, fitting the velocity fields in detail should further constrain the viewing angles and hence the range of possible models. However, since with the current observational errors the velocity data are already consistent with a simple circular velocity field, it will clearly be difficult to discriminate between different triaxial models. For that reason we have restricted ourselves to investigating whether the density profile of a viable triaxial model follows the light profile more closely than it does in the spherical model found in § III. We have considered the following two representative cases, each of which is indicated in Figures 8 and 9b:

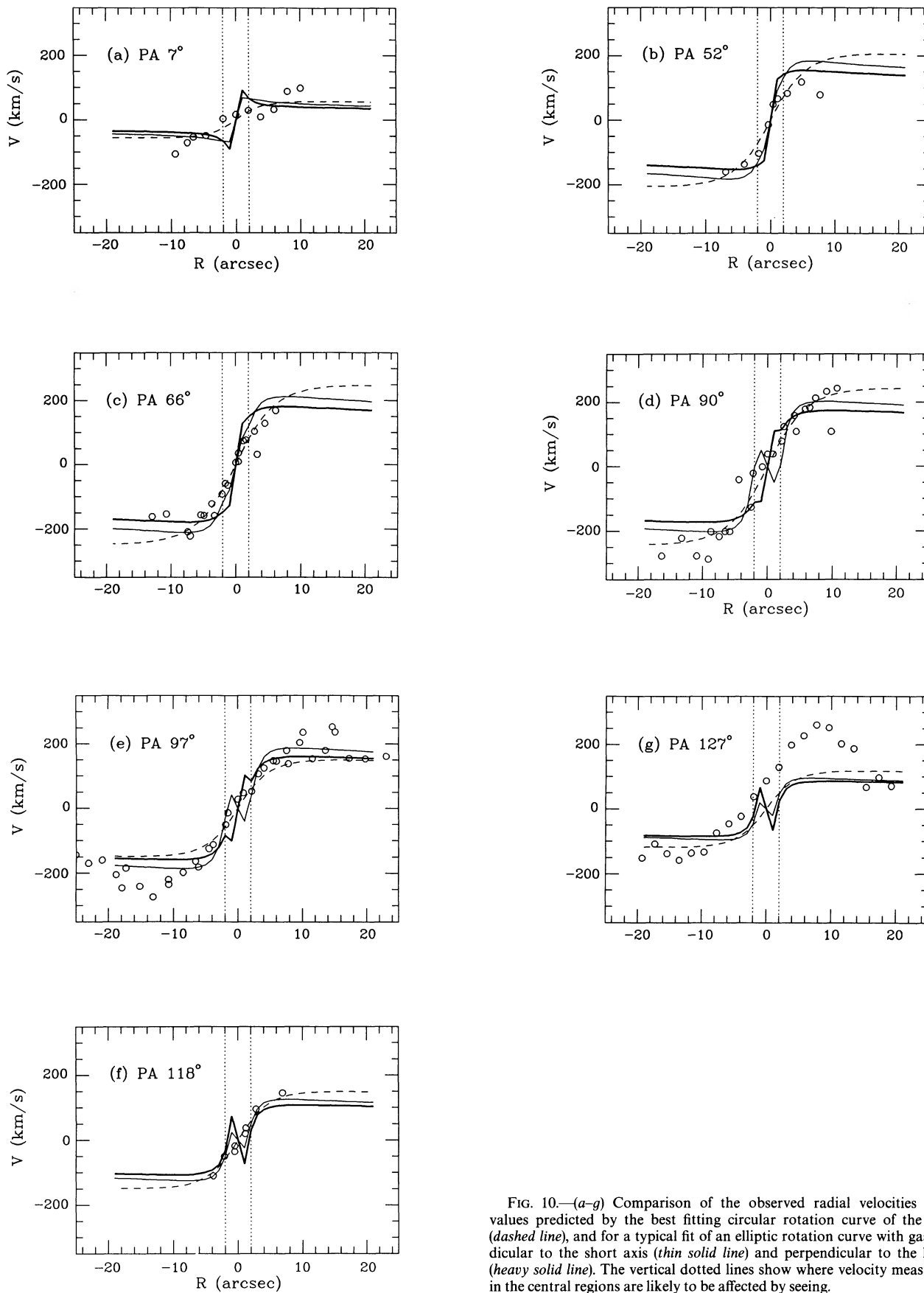


FIG. 10.—(a-g) Comparison of the observed radial velocities with the values predicted by the best fitting circular rotation curve of the form (1) (dashed line), and for a typical fit of an elliptic rotation curve with gas perpendicular to the short axis (thin solid line) and perpendicular to the long axis (heavy solid line). The vertical dotted lines show where velocity measurements in the central regions are likely to be affected by seeing.

1. A near-oblate triaxial model with central axis ratios of 0.92 and 0.54, seen at $\theta = 52^\circ$ and $\phi = -39^\circ$, with the gas on elliptic orbits in the plane perpendicular to the longest axis.
2. A near-prolate triaxial model with axis ratios 0.51 and 0.44, viewing angles $\theta = 52^\circ$ and $\phi = -13^\circ$, and the gas on elliptic orbits in the plane perpendicular to the shortest axis.

In both cases we calculated the model velocity field by means of equations given in dZF, and fitted it to the data, keeping θ , ϕ , and the central axis ratios fixed, but with A , c_0 , and p as free parameters. The best fitting values, which should be considered as representative, are listed in Table 6. Figure 10 shows the model curves and the observed velocities along the seven position angles. Outside the central $2''$ the agreement is generally quite good. The fit is not very good at P.A. 127° , which is not surprising in view of the remarks made at the end of § 3.1.

In the center there are rapid velocity shifts because the elliptic closed orbits become very elongated. As explained in dZF, this is the case for any nonrotating triaxial galaxy with a finite core radius. As a result, shocks will occur, and the approximation that the gas is on simple closed orbits breaks down. Because of this, the gas velocity dispersion should rise steeply in the inner few arcseconds, as apparently (if the line broadening is intrinsic and not caused by unresolved rotation) observed in NGC 5077. The observed velocities are also influenced by seeing in the central $2-3''$, so that one should not expect the observations to be well fitted by our simple model in the central few arcseconds.

The derived values of the core radius c_0 in the triaxial velocity fits are smaller than those found with the circular fit in § 3, as may be seen from Table 6. Figure 11 shows the corresponding density profiles along the intermediate axis, calculated by means of the equations given in Appendix B of dZF. Also shown is the luminosity profile along the intermediate axis of a triaxial model of the kind (6) with a de Vaucouleurs profile. This has been normalized to have the same total luminosity as the spherical de Vaucouleurs model used in § 3. For the prolate triaxial model, M/L is roughly constant at a value of 4.5 over the whole observed range. The oblate triaxial model has a slightly larger core, but M/L is still essentially constant outside the central $2-3''$, and equal to ~ 3.5 .

The constant M/L models are possible because the misalignment angle of 23° is consistent with values of ϕ which are close to zero (especially for the models with the gas perpendicular to the shortest axis), so that the elliptic orbits are seen nearly broadside on and the gas velocities appear to rise slowly even though the core radius of the mass distribution is small. Since the gas at the tangential point is observed nearly at the apocenter of its orbit, the line-of-sight velocity is relatively low. In a spherical model this is interpreted as a low circular velocity, which is attributed to a low mass inside the orbit, so that the inferred M/L is low. At large radii, the gas orbits in the triaxial models become nearly circular.

It is well known that the circular velocity at a given radius is larger for a flattened model than for a spherical model with the same mass (Binney & Tremaine 1987). Thus we expect the mass of our triaxial model inside the outermost data point to be less than the mass of our spherical model. As we have just seen, the density profile inferred from the spherical model lies below that of the triaxial

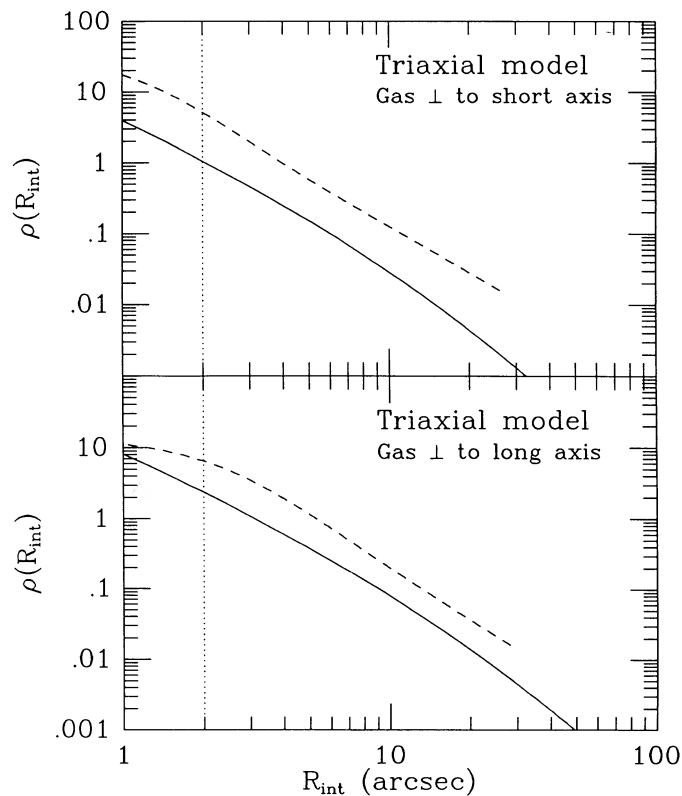


FIG. 11.—Density profiles for the two triaxial models listed in Table 6 (shown by dashes for gas in the plane perpendicular to the short axis and by dots for gas in the plane perpendicular to the long axis) and the luminosity density distribution derived from the best-fitting de Vaucouleurs profile (solid line).

model in the central regions, so the density profile of the spherical model should lie well above that of the triaxial model at large radii, in order to generate a larger total mass. A comparison of Figures 7 and 11 shows that this is indeed the case.

Finally, given the uncertain inclination of the gas disk in NGC 5077, one might ask whether the inclination of 52° adopted in our models yields a reasonable value for the maximum *deprojected* rotation velocity, V_{\max} . For the models in Table 6, and with the gas disk viewed exactly edge-on, we have $V_{\max} = 327 \text{ km s}^{-1}$ for the circular model and 275 km s^{-1} for the triaxial models. We have compared these values with the maximum rotation velocities for the bulges of the 10 Sa galaxies with rotation curves measured by Rubin et al. (1985) and luminosity profiles determined by Kent (1988). The total magnitude of each galaxy (from the Revised Shapley-Ames Catalog (RSA), Sandage & Tammann 1981) was converted to a bulge magnitude using the bulge-to-total luminosity ratio B/T tabulated by Kent. We find that our derived V_{\max} for NGC 5077 (which has $M_B^0 = -21.03$ in the RSA) falls within the range covered by spiral bulges of similar luminosity.

5. A MODEL WITH A WARPED POLAR RING

We now relax the assumption that the gas in NGC 5077 is coplanar and consider the case of a warped polar ring. We make two assumptions in modeling systems of this kind: (1) the galaxy is oblate and (2) the disk has a hole in the center so that gas seen near the nucleus is actually at larger radii.

An initially planar gas disk inclined to the equator of an oblate galaxy becomes distorted in two ways: the gas orbits precess differentially about the pole of the galaxy so that the disk becomes twisted in a *leading* sense relative to its rotation, and the self-gravity of matter in the disk causes it to warp up *toward* the pole with increasing radius. This warping naturally leads to an "S" shape like that seen in the $H\alpha$ contours. If the disk is massive enough, there may be equilibrium states in which self-gravity holds the disk together against differential precession (Sparke 1986). We constructed two sets of models for NGC 5077, one with the ring in equilibrium and one in which it evolves with time.

The rotation curve of the galaxy is approximated by

$$V(r) = 300\sqrt{1 - (a/r) \arctan(r/a)} \text{ km s}^{-1}, \quad (8)$$

where the core radius a is taken as $1''$; $V(r)$ rises to two thirds of its asymptotic value within $2''$. This simple form is chosen so that the model rotation curve rises at least as steeply as that implied by constant M/L for the stars; we aim to show that the observed rotation curve should rise much more slowly. Because the galaxy potential is flattened, orbits precess about the pole of the galaxy at a rate

$$\dot{\phi} = \frac{3V(r)}{4r} \eta \cos \vartheta, \quad (9)$$

where ϑ is the angle between the orbit and the equatorial plane and η is the flattening of the potential. The density distribution is about three times as flat as the potential; we take $\eta = 0.1$ here, which is appropriate if NGC 5077 (an E3 galaxy) is seen nearly edge-on. The effect of this small oblateness on the shape of the gas orbits is neglected.

We have measured a mass $3 \times 10^9 M_\odot$ of neutral hydrogen in the galaxy. Assuming by analogy with polar ring systems (van Gorkom, Schechter, & Kristian 1987) and with the galaxy Centaurus A (van Gorkom 1987) that this gas is entirely associated with the ring implies a ring mass of at least $4.2 \times 10^9 M_\odot$ allowing for the mass of primordial helium. The ring is modeled as a set of concentric massive wires, representing gas on near-circular orbits. Each of these can precess in the gravitational field of the other wires and of the oblate galaxy; the equations of motion are the same as in Sparke (1986).

Calculations were made in a system where the unit of length is $10''$, velocities are measured in units of 100 km s^{-1} and the mass scale is given by setting the gravitational constant $G = 1$. With $H_0 = 50 \text{ km s}^{-1} \text{ Mpc}^{-1}$, the mass unit is $6.35 \times 10^9 M_\odot$ and time is measured in units of $2.65 \times 10^7 \text{ yr}$. The ring mass was taken as 0.7 units ($4.45 \times 10^9 M_\odot$).

We have made no attempt at a formal fit of models to observations but have selected models which appear to match the data. The viewing angle was chosen by requiring the models to reproduce the appearance of the observed $H\alpha$ contours. No central hole is seen in the gas, so the model disk must somewhere turn edge-on to the observer. To produce regions of high surface density which might correspond to the bright knots near P.A. 52° , this radius should be between $5''$ and $10''$. The position angle of the line of nodes of the ring (where it crosses the plane of the sky) must twist from $\sim 45^\circ$ to the galaxy major axis at around $7''$ radius and must lie approximately along the minor axis further out.

5.1. Equilibrium Models

The polar ring is massive enough that a stable equilibrium can be maintained by self-gravity. One such model is illustrated in Figure 12; the ring has a central hole of $7''$ radius, then a surface density decreasing exponentially with scale length $10''$ out to $15''$ radius. The mass distribution in the ring cannot be derived from its surface brightness in $H\alpha$, since the ionized gas contributes very little of the total mass; the results of the modeling are not sensitive to the exact form assumed for the surface density, and an exponential is used for convenience. Figure 12a shows the gas orbits when the system is viewed from the equatorial plane of the galaxy; the ring is tilted with respect to the galaxy pole and warps up toward the pole with increasing radius. There is no differential precession, so the ring is not twisted about the galaxy pole (Sparke 1986). Thus if it is viewed from the equatorial plane, all the gas orbits will have nearly the same inclination to the line of sight; instead, the $H\alpha$ contours suggest that the outer part of the ring must be nearer to face-on. Figure 12b shows a view at 30° from the equator, such that the innermost orbit is seen exactly edge-on. Now the gas orbits follow a shape like that of the $H\alpha$ contours, twisting toward the minor axis, and becoming more nearly face-on, with increasing radius.

Because the gas seen in projection close to the galaxy center is in fact further away and because the orbits twist with radius, the

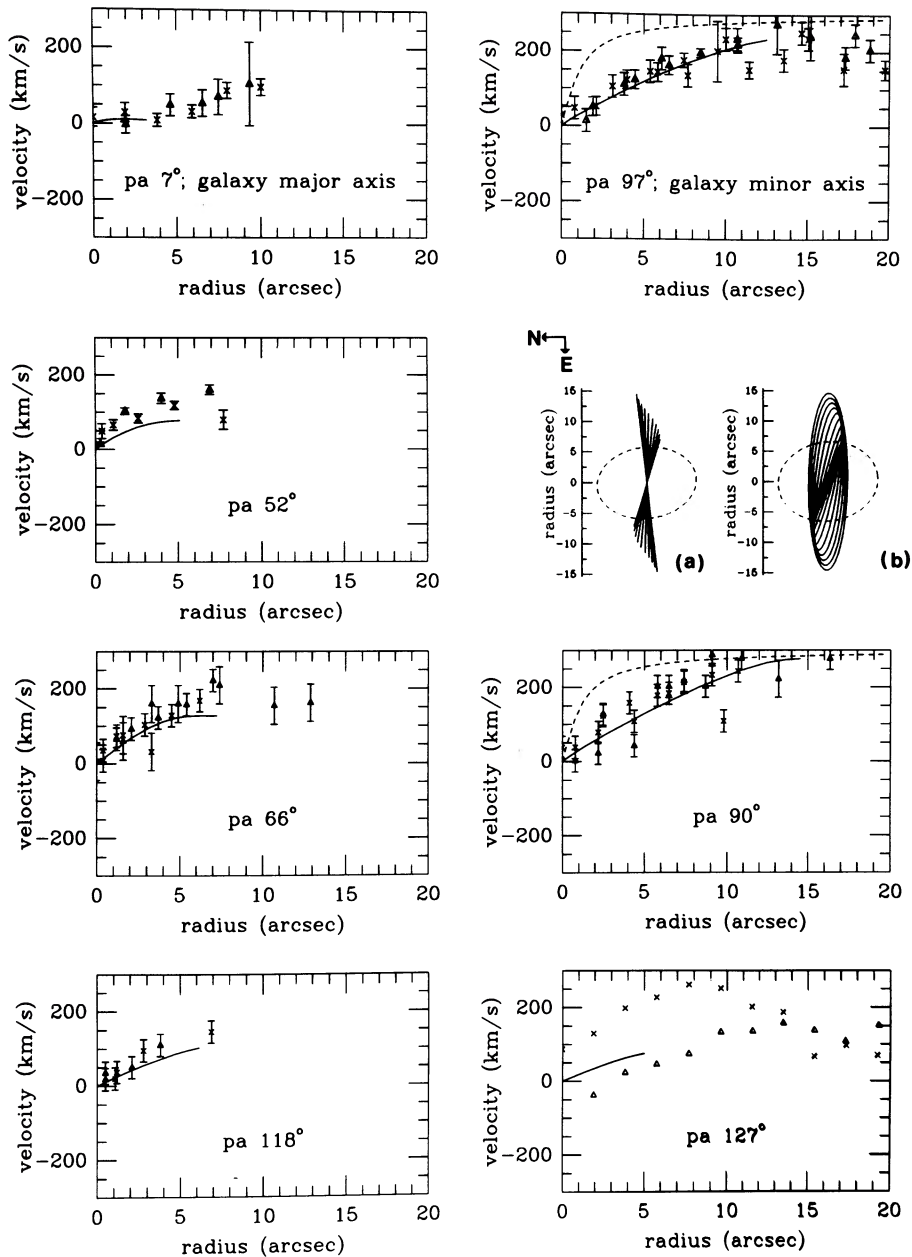


FIG. 12.—Equilibrium model for a polar ring in an oblate galaxy potential. Comparison of the observed radial velocities with those predicted by the model viewed in orientation (b); the two sides of the rotation curve are shown by the different symbols. The assumed true rotation curve of the galaxy is shown by the dashed line in the panels for P.A. 90° and P.A. 97°. The inset pictures show orbits of gas in the ring (a) as seen from the galaxy equatorial plane and (b) at 30° from the equator, with the innermost orbit exactly edge-on. The dashed line shows an isophote of the galaxy, assumed to be intrinsically E3.

velocities predicted along the galaxy minor axis at P.A. 97° rise much more slowly than the assumed rotation curve (*dashed line*). The model gives a reasonable fit to the measured radial velocities, except close to the major axis of the galaxy at P.A. 7°—the gas orbits are too nearly edge-on to fit either the major-axis velocities or the shape of the H α contours. Tilting the galaxy pole further away from the observer takes the outermost orbits more face-on but reduces the swing in position angle. A model with an intrinsic twist about the galaxy pole would fit the observations better; such a twist is the inevitable result of different precession in a time-evolving ring.

5.2. Time-evolving Model

We constructed a time-dependent model in the same way, starting with the gas disk in a plane tilted at 15° to the pole. The assumed density profile of the ring was slightly different; the central hole was decreased to 5".5, in an effort to bring the bright central linear feature to smaller radius, and the density gradient was steepened to an exponential scale length of 5". It was found that if the ring had an outer zone extending to 20" which contained very little mass (and so did not affect the dynamics), the appearance of the

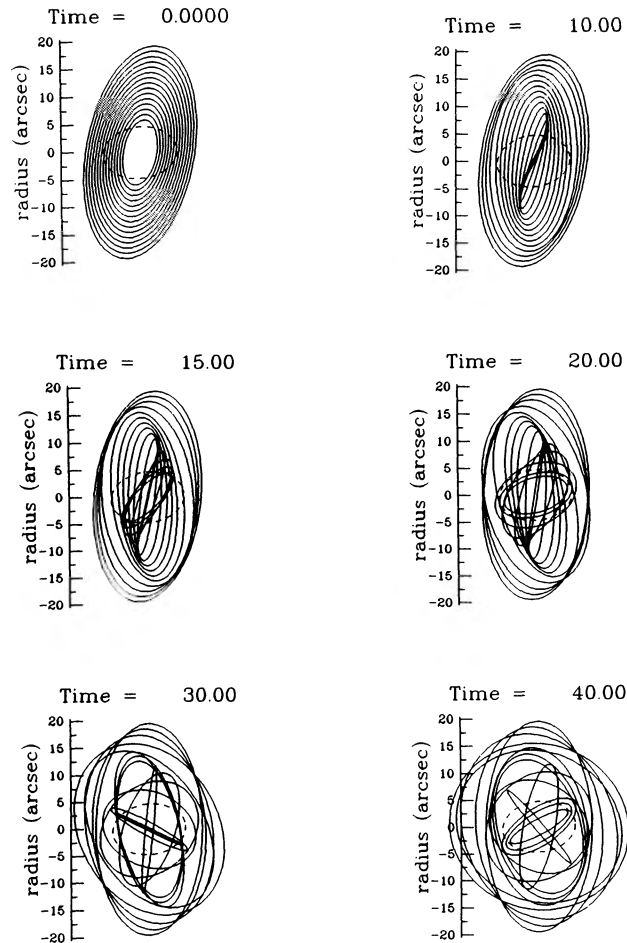


FIG. 13.—Time-evolving polar ring model. The model is viewed from the equatorial plane of the oblate galaxy, such that the outermost orbit is always seen at 30° from edge-on. The dashed line shows an isophote of the galaxy. The time unit is 2.65×10^7 yr, so that time 15 corresponds to 4×10^8 yr.

ring and the fit to the outer part of the radial velocity curves were improved. Thus the density was taken to decrease smoothly between $13''.5$ and $16''.5$, and to be zero outside that region.

Self-gravity is not strong enough to hold this ring model together in its initial coplanar state. Figure 13 shows how the model develops in time; the system is viewed in the galaxy equatorial plane, such that the outer gas is always seen 30° from edge-on. Gas orbits regress differentially in the oblate galaxy potential, so that the ring develops a twist about the pole. Self-gravity causes the massive part of the ring to warp up toward the pole in the same way as the equilibrium model, but the outermost orbits are not much affected by this and remain close to their original inclination. The result is an S-shaped twist, similar to the $H\alpha$ contours; the closest match is at 15 time units, or 4×10^8 yr. Later, the ring breaks up into several disjoint pieces, and by time 40 (or 10^9 yr) it is completely chaotic; no disk structure can be seen and the surface brightness would be much lower.

The radial velocities corresponding to the model at time 15 are shown in Figure 14. Again, because the disk is warped, the observed velocities near the galaxy minor axis (at P.A. 90° and P.A. 97°) rise much more slowly than the actual circular speed (*upper curve*); there is no need to postulate a drop in the mass-to-light ratio. Because the ring is so twisted, lines of sight may intersect the surface 2 or 3 times, so that some of the predicted radial velocities are multivalued. Along P.A. 52° and 66° the model velocities are split by 50 km s^{-1} or more; the rotation of the inner part of the disk fits the observations better than the velocity of the outer gas. This is reasonable, since the outer material is probably fainter and may not show up in the velocity measurements. The model matches the observed velocities quite well except along the major axis at P.A. 7° ; the problem here is that if the gas moves on circular orbits, then both the high velocities along the minor axis and the appearance of the $H\alpha$ contours require that the outer gas orbits are aligned close to the minor axis, so that velocities along P.A. 7° must be small. This discrepancy may be an indication that the gas orbits are significantly elliptical—see below. Changing the viewing angle does not appreciably improve the fit to either the velocities or the shape of the $H\alpha$ contours.

As was pointed out in § 4, polar orbits in an oblate galaxy are elliptical, rather than circular. Including the ellipticity in these models would change the gravitational forces on the rings by an amount comparable to the flattening of the potential, here $\sim 10\%$, which is small compared to other uncertainties. A more significant effect is in changing the fits to the observed velocity field. Speeds on a polar orbit are highest when crossing the galaxy equator and lowest at the pole, so that if ellipticity were included the model rotation speeds would be lower along the major axis of the gas disk (P.A. 97° and 90°), which would tend to improve the fit. When

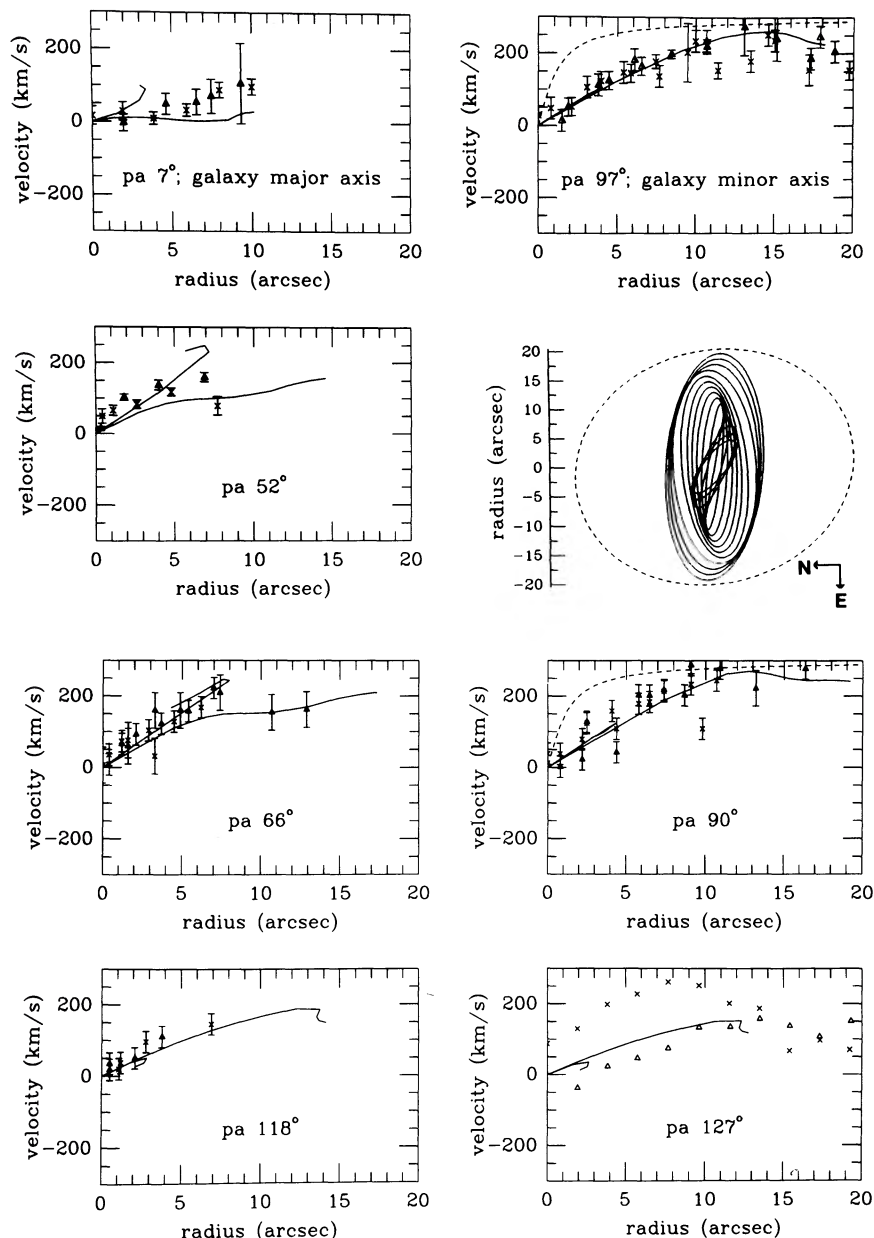


FIG. 14.—Comparison of observed radial velocities with those predicted by the time-evolving model of Fig. 13, viewed at time 15. Symbols are the same as in Fig. 12.

the orbits are elliptical, the line of zero velocity is generally displaced from the minor axis of the light distribution; this would allow a model to have nonzero velocities along the direction P.A. 7° .

This polar ring model suggests that we see the galaxy NGC 5077 fairly near to edge-on, in agreement with the “oblate-triaxial” model of § 4. By contrast, it implies that the ring is young, formed about half a billion years ago. The age estimate depends on our assumptions on how the precession rate changes with radius, and might be significantly increased if the central parts of the galaxy (which are hard to observe because of the ring) are much rounder than the outer regions; this would reduce the differential precession and slow down the ring evolution.

6. OTHER ELLIPTICAL GALAXIES

A few other elliptical galaxies with a gaseous or dusty disk have some kinematic and photometric data available, and it is interesting to see how many of these have slowly rising gas rotation curves. We have taken radial velocity measurements from the literature, fitted these to the functional form (1), as in § 3, and calculated the spherical density profile corresponding to the best fit. In what follows, we briefly discuss each galaxy. Table 7 summarizes the relevant data.

1. *NGC 1947*.—Kinematic observations for this E1 galaxy, which has a minor-axis dust lane, have been reported by Möllenhoff (1982). If we adopt $\Psi_0 = 21^\circ$ and $\theta = 75^\circ$ as suggested by Möllenhoff, we find $A = 317 \text{ km s}^{-1}$, $c_0 = 5.7$ and $p = 1.18$.

2. *NGC 4278*.—This elliptical galaxy with a gas disk was discussed in some detail by DBB, who measured gas velocities at five

TABLE 7
DATA ON GALAXIES

Identification	B mag	v_{sys} (km s^{-1})	D (Mpc)	r_e	r_e (kpc)	M $10^{11} M_{\odot}$	r_{max}	L_T ($10^{10} L_{\odot}$)
NGC 1947.....	11.83	930	19	19"	2.8	0.31	35"	0.97
NGC 4278.....	11.15	659	13	30	1.9	0.37	30	0.85
NGC 5077.....	12.60	2683	56	19	5.2	0.82	36	4.2
NGC 5266.....	12.8	2476	48	65	15.0	1.5	27	2.6
NGC 7097.....	12.6	2596	52	19	4.6	0.38	15	3.6
IC 5063.....	13.05	3210	64	21	6.5	0.38	15	3.6

COL. (2).—B magnitude from de Vaucouleurs, de Vaucouleurs, & Corwin 1976

COL. (3).—Galactocentric systemic radial velocity from the following sources: NGC 1947: Möllenhof 1982; NGC 4278: DBB; NGC 5077: this paper; NGC 5266: Caldwell 1984; NGC 7097: CKR; IC 5063: Caldwell & Phillips 1981.

COL. (4).—Distance, derived from the systemic velocity and a Hubble constant $H_0 = 50 \text{ km s}^{-1} \text{ Mpc}^{-1}$.

COL. (5).—Effective radius from the following sources: NGC 1947, 4278, IC 5063: de Vaucouleurs, de Vaucouleurs, & Corwin 1976; NGC 5077: this paper; NGC 5266: Varnas et al. 1987; NGC 7097: Caldwell, Kirshner, & Richstone 1986.

COL. (6).—Effective radius in kiloparsecs.

COL. (7).—Total mass within the last measured point of the rotation curve of the gas, as given by the spherical model.

COL. (8).—Largest radius for velocity measurements.

COL. (9).—Total B luminosity.

position angles. H I observations have been made by Raimond et al. (1981). Fitting a circular velocity field gives $A = 264 \text{ km s}^{-1}$, $c_0 = 2''.74$, $p = 1.00$, $\Psi_0 = 42^\circ$ and $\theta = 55^\circ$. The kinematic axis may well be misaligned with the photometric axes, although the isophotes of the stellar light are nearly round. As noted by DBB, the gas velocities observed in NGC 4278 agree well with those predicted for a spherical galaxy obeying the $R^{1/4}$ law in projection (see below).

3. *NGC 5266*.—This E4 galaxy has a prominent minor-axis dust lane, and has been studied by Caldwell (1984), Möllenhof & Marenbach (1986), and Varnas et al. (1987). Gas rotation curves are available for seven position angles from 15° to 152° . The rotation curve of the gas continues to rise out to at least $13''$ from the nucleus, and a fit to the available data gives $A = 281 \text{ km s}^{-1}$, $c_0 = 13''.2$, $p = 1.00$, $\Psi_0 = 31^\circ$ and $\theta = 69^\circ$. Varnas et al. showed that the morphology of the gas is consistent with it being in a warped ring around a slowly tumbling triaxial galaxy with the direction of tumbling opposite to that of the stellar streaming. As noted in § 4.1, it is not clear that counter rotation of the stars over a substantial range in radius is possible (Vietri 1988). It should be interesting to do a detailed comparison of the observed velocity field of the gas with that of the model.

4. *NGC 7097*.—This is the E4 galaxy studied in detail by CKR. Fitting the gas with a circular velocity field in a spherical potential, they found an increase of M/L from less than 1 in the central region to ~ 3.5 at the last measured point. From the analysis presented in §§ 4 and 5 of this paper it is evident that this conclusion may have been too hasty. Our fit to the observed velocities along the apparent major axis gives $A = 937$, $c_0 = 6''.7$, $p = 1.5$, $\Psi_0 = 14^\circ$, and $\theta = 55^\circ$. The kinematic axes seem to coincide with the photometric axes.

5. *IC 5063*.—This E2 galaxy has been studied by Caldwell & Phillips (1981) and Danziger, Goss, & Wellington (1981). A fit to the Caldwell & Phillips data gives $A = 297$, $c_0 = 3''.1$, $p = 1.05$, $\Psi_0 = 127^\circ$ and $\theta = 60^\circ$.

Figure 15 shows the deprojected circular rotation curves for the galaxies listed above, scaled such that they have the same effective radii. For comparison, we also show the rotation curve for a de Vaucouleurs law with the same effective radius, with an (arbitrary) maximum velocity of 350 km s^{-1} . Note that this has not been convolved with seeing, so rises more steeply than the observed rotation curves.

Of the six galaxies in Table 7, three (NGC 5077, NGC 5266, and NGC 7097) have gas rotation curves which rise more slowly than expected from a circular model. NGC 1947 may also fall into this class, although the coarser spatial resolution of the available data make this less certain. NGC 4278 and IC 5063 appear to be "well-behaved" galaxies in which the gas velocities follow those predicted by the $R^{1/4}$ law if one makes a reasonable allowance for the effects of seeing. Note that errors in R_e will have some effect on the curves: underestimating R_e will make the rotation curve appear to rise too slowly, while overestimating R_e will make it appear to rise too fast. However, errors of at least 30%–50% would be needed to have any gross effect on the rotation curves in Figure 15.

7. DISCUSSION

There are two main issues. First, what is the most likely explanation for the slowly rising gas velocities in NGC 5077? Second, what implications, if any, does this have for our understanding of the rotation curves of other early-type galaxies?

7.1. Triaxial Models

We have shown that it is possible to construct triaxial mass models with constant M/L which reproduce the gas velocities observed in NGC 5077. These models suggest that NGC 5077 has a constant M/L of ~ 4 –5 in solar units throughout the central 5–10 kpc (for a Hubble constant of $50 \text{ km s}^{-1} \text{ Mpc}^{-1}$). Furthermore, the deprojected gas velocities at large radii (where the orbits are essentially circular) are consistent with those in spiral bulges of similar luminosity.

The velocity fields of the triaxial models fit the existing data somewhat more poorly than the classical spherical model, but they offer several advantages: (1) they can explain the observed position angle difference of 23° between the gas rotation axis and the apparent major axis of the stars as being due to a projection effect, (2) they provide a natural explanation for the observed increase

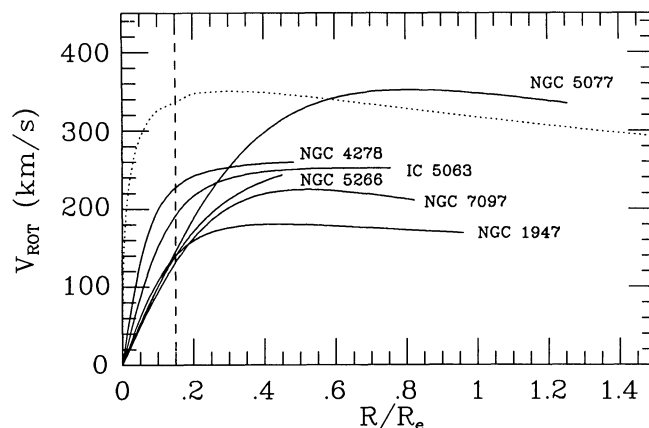


FIG. 15.—Deprojected gas rotation curves for the six elliptical galaxies discussed in § 6. We have assumed $H_0 = 50 \text{ km s}^{-1} \text{ Mpc}^{-1}$, circular rotation and parameters A , c_0 , and p as described in the text. The dotted curve is a theoretical rotation curve for a spherical galaxy following an $R^{1/4}$ law, while the vertical dashed line shows the radius within which velocities are affected by seeing in the case of NGC 5077 (this may be different for the other galaxies, since R_e varies).

in the gas velocity dispersion in the central $2''$ – $3''$, due to strongly noncircular motions, and (3), the associated density distributions have *small* cores, so they do not require M/L to drop to low values in the center.

Triaxial models also offer the hope of explaining in a general way the slow-rising gas rotation curves of other ellipticals (§ 6) and the “massless” bulges of some early-type spirals (Kent 1988). In the triaxial model for NGC 5077, we see slowly rising gas velocities because we happen to observe the elliptic gas disk nearly broadside on, specifically, from closer to the long axis of the galaxy than the intermediate axis if the gas is in the plane perpendicular to the short axis, or from closer to the intermediate axis of the galaxy than the short axis if the gas is in the plane perpendicular to the long axis. In a sample of elliptical galaxies oriented at random, we would therefore expect to see some with slowly rising rotation curves and some with rotation curves which rise *faster* than predicted by the $R^{1/4}$ law (although the “fast-rising” curves may be considerably smeared out by seeing if c_0 is small). It follows that M/L profiles derived from the fitting of circular gas velocity fields should be treated with considerable caution.

It would be interesting to calculate the expected fraction of “slow” and “fast” risers among the general population of ellipticals, but this requires detailed modeling which is outside the scope of the present paper. An extra problem lies in acquiring a sufficiently large and *unbiased* sample of elliptical galaxies with accurately-measured gas velocity fields to investigate the true distribution of intrinsic shapes. Very few nearby ellipticals have emission lines extending beyond R_e , as observed in NGC 5077, and we do not know whether such galaxies are necessarily typical of the elliptical population as a whole. As dZF point out, the amount of radial streaming in a gas disk may depend on the shape of the galaxy potential. If so, elliptical galaxies with stable, long-lived disks (the ones we are most likely to observe) would have potentials of a particularly favorable shape in the plane in which the gas resides and might represent only a special subset of the full range of intrinsic shapes possible for ellipticals.

Slowly rising rotation curves have also been measured along the apparent major axis of many bulges of spiral galaxies (Fillmore, Boroson, & Dressler 1986; Kent 1988). In this case, the gas must lie in the equatorial plane of an oblate or oblate-triaxial bulge, which makes the derivation of the intrinsic shape somewhat easier (Gerhard & Vietri 1986; Bertola, Rubin, & Zeilinger 1989; Gerhard, Vietri, & Kent 1989). It remains to be seen whether one can make spiral bulges sufficiently triaxial to explain the observed fraction of slow and fast-rising rotation curves, but the problem is more tractable than for elliptical galaxies. Work along these lines is in progress.

7.2. Polar Ring Models

We have shown in § 5 that models with the gas in a warped polar ring ring can also explain many of the observed features of NGC 5077, including the twisted shape of the $H\alpha$ disk. This kind of model overcomes the need for a falling central M/L because the ring twists, so that low-velocity gas seen close to the nucleus is actually in a highly inclined orbit at larger radius. The present shape of the ring is transient, and the model implies that the ring formed probably less than a billion years ago. The $H\text{ I}$ mass in NGC 5077 is similar to that in polar ring S0 galaxies (van Gorkom et al. 1987), and a model with a warped polar ring is a viable alternative to the triaxial models outlined in § 4. More accurate, higher resolution velocity data will be needed to distinguish between these two possibilities—in particular to search for line-splitting caused as a line of sight intersects the warped gas layer more than once.

There are, however, some problems with a simple polar ring model for NGC 5077. The emission-line luminosity is highest in the nucleus, and the velocity dispersion of the gas also peaks sharply there. The peak in the dispersion may be partly due to unresolved rotation, especially since the gas orbits must be elliptical and not circular at small radii, but the high central surface brightness suggests that some gas at least is actually *in* the nucleus rather than simply seen in projection. One therefore has to invoke a two-component model for the gas, with a central nonrotating “hot” component ($\sigma_{\text{gas}} \sim 230 \text{ km s}^{-1}$) and a “cold” ($\sigma_{\text{gas}} \leq 50 \text{ km s}^{-1}$) rotating ring further out. These components must also conspire to allow both the integrated gas surface brightness and the gas velocity dispersion to vary smoothly with radius, as seen in Figure 16 (although seeing may help to smear out any discontinuities). The presence of a central “hot” ionized gas component is not unreasonable, since these occur in many bright ellipticals (Phillips et al. 1986) but it makes interpretation of the gas morphology more difficult. A further problem is the observed gas rotation at P.A. 7° , which is difficult to reconcile with the models in § 5, or, indeed, with any ring model where the kinematic minor axis coincides with a photometric axis. This could possibly be remedied by considering a polar ring around a triaxial galaxy.

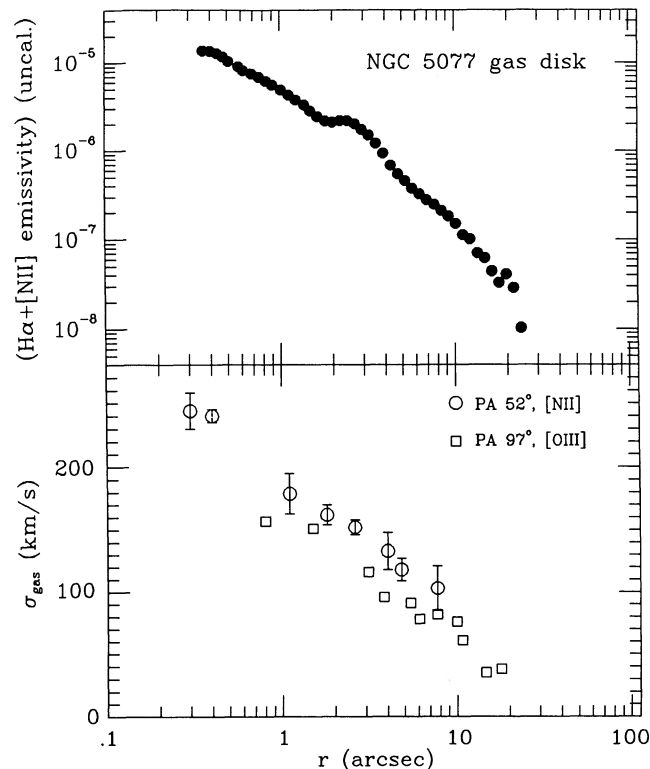


FIG. 16.—(a) Emissivity profile of the ionized gas disk in NGC 5077. The continuum-subtracted emission line image in Fig. 3 was analyzed using the GRASP profile-fitting program to derive the surface brightness of $H\alpha + [N II]$ emission at each radius. (b) Velocity dispersion profile of the ionized gas, measured along P.A. 52° from the $[N II] \lambda 6584$ line (open circles) and along P.A. 97° from the $[O III] \lambda 5007$ line.

If polar rings are common in gas-rich elliptical galaxies, as suggested by the observation that minor-axis dust lanes are more common than major-axis dust lanes in elliptical galaxies (Bertola 1987), then the sort of models discussed in § 5 may also be applicable to elliptical galaxies in general (although not to most spirals). Of the objects in Table 7, three of the four “slow risers” have minor-axis disks (the exception is NGC 7097, where the gas rotates along the major axis). Selection effects may act to increase the fraction of slow risers in any given sample. Gas disks and dust lanes are most likely to be recognized if they are close to edge-on at large radii. Such systems are precisely those in which the gas will warp toward being more face-on in the centre, producing a slow-rising rotation curve. Further, any system where the ring has a central hole will inevitably be a “slow riser.”

7.3. Future Work

We have shown that there are several possible models for NGC 5077 which are consistent with the observations made so far. Further work, both observational and theoretical, is needed to distinguish between these.

On the observational side, we need better and more accurate coverage of the stellar velocity field. Slow rotation ($V \sim 10\text{--}15 \text{ km s}^{-1}$) of the stars in the outer parts is not ruled out by the present data. If the galaxy is indeed rotating (and many of the elliptical galaxies observed by Franx (1988b) rotate very slowly) and we can determine the rotation axis, this will give an extra constraint on the intrinsic shape if we can assume that the rotation axis lies along a principal axis of the galaxy. The caveat here is that in a triaxial galaxy with a nonrotating figure there may be stellar streaming around both the short axis and the long axis, so that the effective observed rotation axis is not necessarily a principal axis of the figure.

Observations with higher spatial resolution will also be useful in confirming the presence of a fast-rotating central core and mapping its velocity field. Our coverage of the gas velocity field is sparse between P.A. -50° and 50° , and more accurate velocities in this region would help us pin down the misalignment angle Θ_* with greater precision. Furthermore, it should allow us to constrain the viewing angles θ and ϕ from the detailed fitting of the velocity field (see dZF). Mapping of the $H I$ disk should give a better idea of the true inclination of the gas, and also offers the exciting possibility of measuring M/L at large radii.

On the theoretical side, we would like to be able to model the behavior of gas disks in rotating triaxial galaxies and to see how the rotating stellar core in NGC 5077 affects the gas velocities near the center. Whereas analytic models based on Stäckel potentials have given considerable insight into the behavior of gas disks in stationary triaxial galaxies with finite core radius, most of the work in the rotating case will need to be done numerically. Even in the nonrotating case it will be useful to construct more detailed models for the gas velocity fields, in particular for cases where there is no core. This should be done not only in the approximation that the gas is on simple closed orbits, but also with state-of-the-art smooth particle hydrodynamic techniques, such as the one developed by Hernquist & Katz (1989).

The stellar velocity dispersions can be related to the potential of the galaxy via the Jeans equations. This is a popular method for spherical galaxies (e.g., Binney & Tremaine 1987) but, with the exception of the work by Bacon (1985) and Fillmore (1986), has not

been applied much to flattened elliptical galaxies. For axisymmetric Stäckel systems the Jeans equations have been solved (Dejonghe & de Zeeuw 1988; Evans & Lynden Bell 1989). The triaxial case is more complicated, but once understood, will allow a systematic study of the relation between the two-dimensional line-of-sight velocity dispersion field and the internal dynamical structure. The results can then be used to deduce further constraints on the intrinsic shape from the observed dispersions. The ultimate goal is to combine the photometry and kinematics of both gas and stars in order to construct dynamical models which allow us to delineate the internal structure of elliptical galaxies.

It is a pleasure to thank J. Binney, N. Caldwell, M. Franx, V. Rubin, M. Schwarzschild, and F. Schweizer for stimulating discussions. G. Galletta kindly took the *B* and *I* CCD images of NGC 5077. Part of this work was done at the Aspen Center for Physics, during the Workshop on Evolution of Galaxies organized by J. Gallagher and D. DeYoung. E. M. S. and F. B. are grateful to the Institute for Advanced Study for its hospitality. This research was supported in part by an RCA Fellowship to T. d. Z.

REFERENCES

- Bacon, R. 1985, *A&A*, 143, 84
 Bender, R. 1988, *A&A*, 202, L5
 Bertola, F. 1987, IAU Symposium 127, Structure and Dynamics of Elliptical Galaxies, ed. P. T. de Zeeuw (Dordrecht: Reidel), p. 135
 Bertola, F., Rubin, V. C., & Zeilinger, W. W. 1989, *ApJ*, 345, L29
 Binney, J. J. 1978, *Comments Ap.*, 8, 27
 ———. 1982, *ARA&A*, 20, 399
 ———. 1985, *MNRAS*, 212, 767
 Binney, J. J., & de Vaucouleurs, G. 1981, *MNRAS*, 194, 679
 Binney, J. J., & Tremaine, S. 1987, *Galactic Dynamics* (Princeton University Press)
 Burbidge, E. M., Burbidge, G. R., & Prendergast, K. H. 1959, *ApJ*, 130, 739
 Caldwell, N. 1984, *ApJ*, 278, 96
 Caldwell, N., Kirshner, R. P., & Richstone, D. O. 1986, *ApJ*, 305, 136 (CKR)
 Caldwell, N., & Phillips, M. M. 1981, *ApJ*, 244, 447
 Contopoulos, G. 1956, *Zs. Ap.*, 39, 126
 Danziger, I. J., Goss, W. M., & Wellington, K. J. 1981, *MNRAS*, 196, 845
 Davies, R. L. 1987, IAU Symposium 127, Structure and Dynamics of Elliptical Galaxies, ed. P. T. de Zeeuw (Dordrecht: Reidel), p. 63
 Dejonghe, H., & de Zeeuw, P. T. 1988, *ApJ*, 333, 90
 Demoulin-Ulrich, M.-H., Butcher, H. R., & Bokserberg, A. 1984, *ApJ*, 285, 527 (DBB)
 de Vaucouleurs, G., de Vaucouleurs, A., & Corwin, H. G. 1976, *Second Reference Catalogue of Bright Galaxies* (Austin: University of Texas Press)
 de Zeeuw, P. T., & Franx, M. 1989, *ApJ*, 343, 617 (dZF)
 de Zeeuw, P. T., & Lynden-Bell, D. 1988, *MNRAS*, 232, 419
 de Zeeuw, P. T., & Pfenniger, D. 1988, *MNRAS*, 235, 949 (dZP)
 Disney, M. J., & Cromwell, R. H. 1970, *ApJ*, 164, L35
 Ekers, R. D., & Ekers, J. A. 1973, *A&A*, 24, 247
 Evans, N. W., & Lynden-Bell, D. 1989, *MNRAS*, 236, 801
 Fillmore, J. A. 1986, *AJ*, 91, 1096
 Fillmore, J. A., Boroson, T. A., & Dressler, A. 1986, *ApJ*, 302, 208
 Franx, M. 1988a, *MNRAS*, 231, 285
 ———. 1988b, Ph.D. thesis, Leiden University
 Franx, M., & Illingworth, G. D. 1988, *ApJ*, 327, L55
 Gerhard, O. E., & Vietri, M. 1986, *MNRAS*, 223, 377
 ———. 1987, IAU Symposium 127, Structure and Dynamics of Elliptical Galaxies, ed. P. T. de Zeeuw (Dordrecht: Reidel), p. 401
 Gerhard, O. E., Vietri, M., & Kent, S. M. 1989, *ApJ*, 345, L33
 Heckman, T. 1980, *A&A*, 87, 152
 Heeschen, D. S. 1970, *AJ*, 75, 523
 Heiligman, G., & Schwarzschild, M. 1979, *ApJ*, 233, 872
 Heisler, J., Merritt, D. R., & Schwarzschild, M. 1982, *ApJ*, 258, 490
 Hernquist, L., & Katz, N. 1989, *ApJS*, 70, 419
 Humason, M. L., Mayall, M. U., & Sandage, A. R. 1956, *AJ*, 61, 97
 Hummel, E., Kotanyi, C. G., & Ekers, R. D. 1983, *A&A*, 127, 205
 Illingworth, G. D., & Franx, M. 1989, In *Dynamics of Dense Stellar Systems*, ed. D. R. Merritt (Cambridge University Press), p. 13
 Jedrzejewski, R. I. 1987, *MNRAS*, 226, 747
 Jedrzejewski, R. I., & Schechter, P. L. 1988, *ApJ*, 330, L87
 Kent, S. M. 1988, *AJ*, 96, 514
 Kondrat'ev, B. P., & Ozernoy, L. M. 1979, *Soviet Astr. Letters*, 5, 37
 Kormendy, J., & Illingworth, G. 1982, *ApJ*, 256, 460
 Kormendy, J., & Westpfahl, D. 1989, *ApJ*, 338, 752
 Magnenat, P. 1982, *A&A*, 108, 95
 Merritt, D. R., & de Zeeuw, P. T. 1983, *ApJ*, 267, L19
 Möllenhoff, C. 1982, *A&A*, 108, 130
 Möllenhoff, C., & Marenbach, G. 1986, *A&A*, 154, 219
 Oort, J. H. 1965, in *Galactic Structure, Stars and Stellar Systems*, Vol. 5, ed. A. Blaauw & M. Schmidt (University of Chicago Press), p. 455
 Phillips, M. M., Jenkins, C. R., Dopita, M. A., Sadler, E. M., & Binette, L. 1986, *AJ*, 1, 1062
 Raimond, E., Faber, S. M., Gallagher, J. S., & Knapp, G. R. 1981, *ApJ*, 246, 708
 Rubin, V. C., Burstein, D., Ford, Jr., W. K., & Thonnard, N. 1985, *ApJ*, 289, 81
 Sadler, E. M., & Whiteoak, J. B. 1991, in preparation
 Sandage, A., & Tammann, G. A. 1981, *A Revised Shapley-Ames Catalog of Bright Galaxies* (Washington, DC: Carnegie Institution)
 Sparke, L. S. 1986, *MNRAS*, 219, 657
 Stark, A. A. 1977, *ApJ*, 213, 368
 Tohline, J. E., Simonson, G. F., & Caldwell, N. 1982, *ApJ*, 252, 92
 Valdes, F. 1986, in *Instrumentation on Astronomy VI*, ed. D. L. Crawford (Proc. SPIE, 627), 749
 van Albada, T. S., Kotanyi, C. G., & Schwarzschild, M. 1982, *MNRAS*, 198, 303
 van der Kruit, P. C., & Allen, R. J. 1978, *ARA&A*, 16, 103
 van Gorkom, J. 1987, IAU Symposium 127, Structure and Dynamics of Elliptical Galaxies, ed. P. T. de Zeeuw (Dordrecht: Reidel), p. 421
 van Gorkom, J. H., Schechter, P. L., & Kristian, J. 1987, *ApJ*, 314, 457
 Varnas, S. R., Bertola, F., Galletta, G., Freeman, K. C., & Carter, D. 1987, *ApJ*, 313, 69
 Vietri, M. 1988, private communication
 Wrobel, J. M., & Heeschen, D. 1984, *ApJ*, 287, 41
 Young, P. J. 1976, *AJ*, 81, 807